Exploration of the Effects of Environmental Factors on the Parameters Needed for the Calculation of the Maximum Pit Size for Stainless Steels 304L and 316L

A

Thesis

Presented to
the faculty of the School of Engineering and Applied Science
University of Virginia

---

in partial fulfillment
of the requirements for the degree

Master of Science

by

Caitryn Bell

May 2022

APPROVAL SHEET

This

Thesis

is submitted in partial fulfillment of the requirements
for the degree of

Master of Science

Author: Caitryn Bell

This Thesis has been read and approved by the examing committee:

Advisor: Robert Kelly

Advisor:

Committee Member: Bicheng Zhou

Committee Member: Richard Martukanitz

Committee Member:

Committee Member:

Committee Member:

Committee Member:

Accepted for the School of Engineering and Applied Science:

Jennifer L. West, School of Engineering and Applied Science

May 2022

Abstract

Once nuclear fuel has been used, it gets stored into stainless steel canisters that are exposed to dry storage conditions. Over time, these canisters are susceptible to corrosion. The maximum pit size model is being used as an input to determine the location-specific risk to failure during the service life of these canisters. In order to estimate the largest pit size possible, important parameters are needed, such as the corrosion potential, repassivation potential, pit stability, and the conductivity of the electrolyte.

In this work, OLI Studio: Corrosion Analyzer^{TM} was used to calculate parameters for a variety of single salt solutions for stainless steels 304L and 316L. OLI was used to study salt solutions based on different degrees of saturation of stoichiometric dissolution of the alloys to better understand the process that occurs inside the active pits. Evans diagrams were extracted for those conditions to further understand the extent to which reactions control the outcome.

In conclusion, it was computationally determined that compounds that have equivalent chloride concentrations will produce the same or similar result. It was found that when the surface solution chemistry changes, the corrosion morphology does as well. At critical, higher temperatures, sharp transitions in the corrosion potential for stainless steel 304L will occur and will result in the corrosion potential being lower than the repassivation potential. Therefore, when the canister reaches a high enough temperature, it will change the corrosion attack from pitting to active, uniform corrosion. When comparing the two databases, it shows that the model used for stainless steel 304L and the inputs for the maximum pit size predictions are sensitive to the parameters used.

Acknowledgments

First, I would like to acknowledge God because none of this would be possible without Him.

I would like to thank my advisor, Dr. Rob Kelly, for giving me this incredible opportunity to work with him. I greatly appreciate how much you have helped me and all the advice you have given me over the years. It was truly a pleasure. I would also like to thank my committee members: Dr. Richard Martukanitz and Dr. Bicheng Zhou.

I would like to acknowledge those in the Kelly group (Dr. Danyil Kovalov, Dr. Ryan Katona, Rebecca Marshall, Duane Macatangay, Petro Atz Dick, Carolina Moraes, Utibe-Eno Charles-Granville, Victor Kontopanos, and Armando Shehi) and the rest of the students in the Materials Science & Engineering department for all of their support. I would like to specifically thank Dr. Ryan Katona, for teaching me how to run the programs and answering all the questions that I had, and Rebecca Marshall, for always helping me when I needed it.

I would also like to acknowledge my family, especially my husband Josh, Danny, Suzanne, and Mimi. I greatly appreciate all the love, support, and encouragement you have shown me over the years. It is such a blessing to be a part of an amazing and loving family. I can never thank you enough for everything that you have done for me.

Financial assistance from the U.S. Department of Energy’s Nuclear Energy University Program under contract DE-NE0008901 is also gratefully acknowledged.

Table of Contents

List of Figures

1. Introduction

1.1 Nuclear Fuel Storage

Nuclear fuel is being used every day to generate electricity. In 2020, the nuclear power plants in the United States (U.S.) generated 790 million megawatt hours (MWh) of electricity which marked the first time that coal-fired electricity was not the largest or second-largest in annual electricity generation[1]. After nuclear fuel has been used, it will remain in the spent fuel pool for several years until it has cooled. Once cooled, the spent nuclear fuel (SNF) is removed and stored inside dry storage canisters before being transported to a permanent repository[2,3]. The U.S. Nuclear Regulatory Commission (NRC) issued licenses for independent spent fuel storage installations (ISFSIs) where the SNF will be stored for 20 years. However, since the U.S. does not have a permanent repository, the fuel will have to remain in dry storage for more than 20 years, past the original license.

These canisters are primarily made of austenitic stainless steels (SS) which include 304 SS, 304L SS, and 316L SS[3]. SS are used because these alloys have thin passive films that naturally form on the surface and decrease the corrosion rate. Unfortunately, these passive films are vulnerable to localized breakdown which will cause the metal to have an accelerated dissolution that can result in corrosion and in the formation of pits[4]. Additionally, many canisters are near salt sources, such as oceans, so there is concern about corrosion damage leading to cracking and therefore, there is a need to determine the location-specific risk to failure during their service life.

1.2 Corrosion of Nuclear Fuel Storage Containers

After a certain period of time, dust will deposit on the surface of the dry storage canisters. As the canister cools, the relative humidity (RH) will increase and salts within that dust will deliquesce to form high chloride concentration in solution. As further cooling occurs, the solution becomes less concentrated, but more salt is deposited, allowing corrosion to occur.

These SS canisters are susceptible to pitting corrosion and stress corrosion cracking (SCC) if sufficiently high internal stresses occur[5]. Pitting corrosion is when the attack is initiated on an open surface and will only occur when there are aggressive anionic species, like chloride ions, present[4]. High concentrations of chloride ions can cause pitting corrosion to occur at room temperature[5].

SCC is a crack formation as a result of stress and exposure to a corrosive environment and has the ability to compromise the structural integrity of the canister[3,4]. Previous studies have discovered that the SCC susceptibility of the canisters was correlated to the deliquescence of the deposited salt, which are mainly composed of sodium chloride and magnesium chloride[3]. When there is an accumulative deposition of these chloride ions, the canisters can develop localized corrosion and can further lead to SCC when residual stress is present[6]. SCC can even occur in SS when there are low concentrations (around 100 ppm) of chloride ions because chloride ions will accelerate the SCC[5].

1.3 Mixed Potential Theory

The mixed potential theory (MPT) is used to predict the corrosion rate of alloys and metals. The theory is that electrochemical reactions must consist of at least two partial cathodic and anodic reactions and that there cannot be any charge accumulation during the reaction[7]. A cathodic reaction is where the reduction occurs (where the cathode acts as an electron acceptor) and an anodic reaction is where the oxidation reaction occurs (where the anode acts as an electron donor)[8].

Consider the reactions below:

(i) $Zn \rightarrow Zn^{2+} + 2e^-$ (anodic)

(ii) $2H^+ + 2e^- \rightarrow H_2$ (cathodic)

Figure 1 shows the diagrams of the potential versus the current density (or corrosion rate) before and after the polarization of the anodic and cathodic reactions. Figure 1a shows that these reactions occur on the surface at the same time and each reaction has its own electrode potential and exchange current density. Figure 1b shows the polarization of each electrode potential to an intermediate value, known as the corrosion potential (E_{corr}) or open circuit potential (OCP)[9].

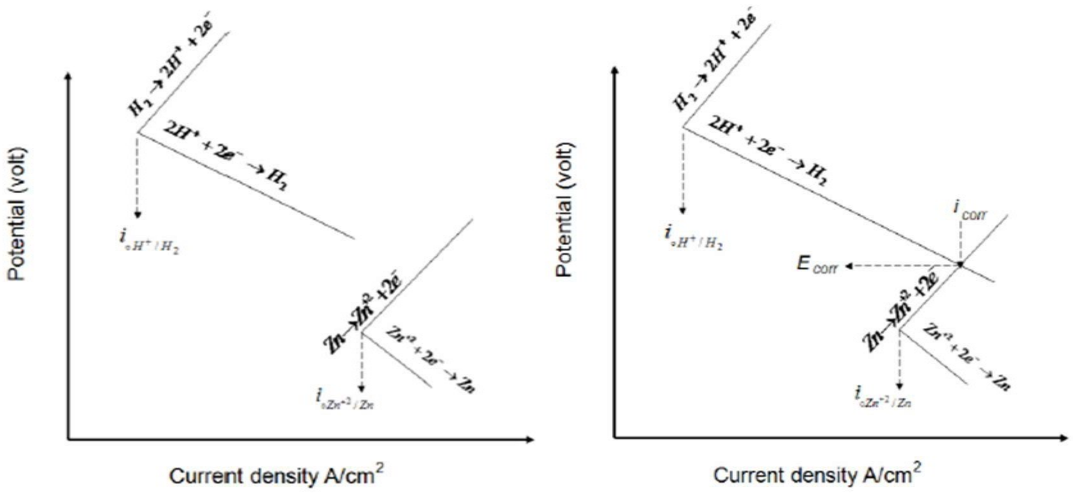

Figure 1: Before (a) and after (b) polarization of anodic and cathodic reactions[9]

1.4 Localized Corrosion of Stainless Steels

Overview

Corrosion is defined as the deterioration of a metal as a result of the reaction to the environment. In order for corrosion to occur, there needs to be an anode, a cathode, an ionic current path, and an electrical path between the two[10]. There are multiples types of corrosion, two of which are general and localized corrosion. General corrosion, or uniform corrosion, is the most common type of corrosion that takes place evenly on the surface of the metal in a corrosive environment, resulting in a smooth look[11,12]. This type of corrosion is often able to be predicted, managed, and even prevented. Localized corrosion is a type of corrosion that specifically targets an area of the metal and is characterized by a rapid attack of a passive metal at localized sites on the surface, due to the breakdown of the passive film, while the rest of the surface is corroding at a slower rate[13]. There are two types of localized corrosion which include pitting (where the attack is initiated on the open surface when there are aggressive anionic species present that results in a small hole or pit) and crevice corrosion (where the attack is initiated at the blocked site)[4].

The process of localized corrosion can be broken down into three main stages. The first stage is initiation, which is the result of the protective passive film breaking down. The second stage is metastable growth, which is where the growth of the majority of pits will stop. The third and final stage is the stable growth, where the sites of localized corrosion can become large in size. It has been determined that localized corrosion will initiate above a critical potential and will repassivate below a lower potential[13]. The repassivation potential, E_{rp}, is the potential at which a pit will stop growing as it will not be able to dissolve fast enough to prevent dilution and any existing pits will repassivate[14]. The phenomenology of localized corrosion can be characterized as scarcity on the surface, high local dissolution rates, and the existence of a repassivation potential.

Although models have been developed to study localized corrosion, several challenges still remain. The first stage, initiation, is very difficult to predict as it has a large stochastic component and initiation events are scarce. Propagation, which describes growth to sizes that could serve as crack starters, is also hard to predict and model. Additionally, time-transient modeling of decades of damage accumulation has not yet been successfully accomplished[13]. An alternative to the immense challenge of time-transient modeling is the development of bounding values for pit size that can be defended as controlled by physical limits.

Maximum Pit Concept

The maximum pit size is created when the size of the features of localized corrosion increase to a point where it needs a cathode current that it cannot get from the surrounding environment[15]. The maximum pit size has been modeled in order to calculate the largest possible pit that can form on a material exposed to a given environment resulting in the formation of a thin electrolyte film. It is useful to calculate the maximum pit size because it provides an upper bound on the size that can determine what parts of the parameter space (such as RH, temperature (T), and loading density (LD)) that could be of concern for allowing a pit of sufficient size to grow that could lead to cracking.

Based on the application of the Mixed Potential Theory, Chen and Kelly developed a computational model of the bounding conditions for localized corrosion, under thin electrolyte films, in order to predict the maximum pit size. An analytical expression was created and validated where the maximum cathode current that could support pit growth was determined and coupled with an expression for the minimum anodic current required for the pit to retain its aggressive solution. The aggressive solution is formed when the dissolution products hydrolyze, attracting chloride ions, leading to a low pH, high chloride concentration environment. The pit stability criterion is the current density required to be generated by a pit at a certain depth and if there is insufficient current density, it will not meet the pit stability criterion and the pit will repassivate. It was found that the maximum pit size in 304 and 316 SS under atmospheric conditions could be predicted by linking the capacity of the cathode to the pit stability criterion[10].

A galvanic couple is a corrosive cell that happens when there is a potential difference that occurs between two different metals or two different locations on the same metal[16]. In pitting corrosion, there are two parts of the galvanic couple which is the anodic pit and the surrounding cathode where the anodic pit is dissolving and the surrounding cathode is covered by a thin film of electrolyte[17]. In order to calculate the maximum pit size, the pit stability product, repassivation potential, and cathodic kinetics need to be determined[15]. Chen and Kelly determined that the lowest repassivation potential for pit propagation is at the pit mouth and chose to use that for the repassivation potential which is always found in the activation-controlled region of the cathodic kinetics[10]. By applying the maximum pit size model to the materials and conditions of the dry storage canisters, it would allow for the identification of the specific parameter combinations (such as the LD, T, RH, salt mixture, and stainless steel of interest as a function of time) that are needed in order to predict the time where the largest pit could be and it could be used to determine the location-specific risk to failure of the canisters during their service life.

1.5 Anderko's and Young's Model

Anderko and Young developed a model that can calculate the corrosion rates of carbon steels. It is composed of a thermophysical module, to produce the realistic evolution of aqueous systems, and an electrochemical module, which includes halide adsorption as it influences the process of corrosion, for the partial anodic (oxidation) and cathodic (reduction) processes that take place on the surface of the metal. The model has been verified with the computed and experimental corrosion rates and has been added to a program, now known as the OLI Studio: Corrosion Analyzer™, where it can analyze the effects that flow velocity, what the solution is composed of, pH, T, and pressure have on the rates of corrosion. Therefore, the model can be used to predict the rates of corrosion and provide a means of calculating E_{rp} and OCP for complicated and concentrated systems that may not have any available experimental data[18,19].

1.6 OLI Software

OLI Studio: Corrosion Analyzer^{TM} is a software program that can be utilized as a predictive tool. It contains two modules, thermophysical and electrochemical, where it is able to predict the general corrosion rates and corrosion and repassivation potentials by modeling the surface reactions, transport phenomena, and bulk chemistry. The thermophysical module is able to determine the concentrations of the reacting species along with the transport and activity properties whereas the electrochemical module mimics the oxidation and reduction processes that occur on the metal surface[20].

These data are required as input for the maximum pit calculations for the dry storage canisters. Conditions under which the repassivation potential is less than the corrosion potential are those for which localized corrosion is expected to be able to propagate, whereas those for which the corrosion potential is lower than the repassivation potential, localized corrosion would not be expected.

1.7 Objective Statement

The main goal of this thesis is to computationally explore the effects of environmental factors on the parameters needed for the calculation of the maximum pit size for 304L and 316L SS.

2. Methods

2.1 OLI Studio Software

How It Was Used

OLI Studio: Corrosion Analyzer^{TM} (version 10.0.1) was used to calculate the corrosion rate, repassivation potential, and corrosion potential for stainless steels of grade 304L and 316L exposed to a wide range of chloride, nitrate, and sulfate solutions at different temperatures. OLI was used to study salt solutions based on different degrees of saturation of stoichiometric dissolution of the alloys to better understand the process that occurs inside the active pits. Evans diagrams were also extracted for these conditions to understand the extent to which different reactions control the outcome.

Database

In OLI, there are a total of three databases that can be used which are aqueous (AQ), the Mixed Solvent Electrolytes (MSE), and the Mixed Solvent Electrolyte-Soave Redlich Kwong (MSE-SRK). The AQ database is OLI's original activity coefficient model. The MSE and MSE-SRK databases are relatively new and are currently limited in the number of species it has as the AQ database contains 6,000 species, the MSE database contains 3,500 species, and the MSE-SRK database is even smaller with no species approximation stated[21]. Therefore, the AQ database was used for the computational calculations in OLI.

Parameters

The parameters used in the OLI Studio: Corrosion Analyzer^{TM} are stream amount, temperature, pressure, and inflows. Unless a temperature study is conducted, the temperature will be at 25°C and the pressure at 1 atm. The inflows comprise of the compound being tested (which will be stated for each calculation in the results section) along with the compounds found in the atmosphere and their amounts which are 55.5082 mol H_2O, 0.209476 mol O_2, 0.780840 mol N_2, 3.14000e^{-4} mol CO_2, 9.340003e^{-3} mol Ar, 1.81800e^{-5} mol Ne, 2.00000e^{-6} mol CH_4, 5.24000e^{-6} mol He, 1.14000e^{-6} mol Kr, 5.000000e^{-7} mol H_2, and 8.700000e^{-8} mol Xe. These values represent the composition of ambient air.

Tests Conducted

The calculations that were made included: corrosion rate versus concentration of the compound, OCP and E_{rp} versus concentration of the compound, corrosion rate versus temperature, and OCP and E_{rp} versus temperature. The range for the compound concentration was from 0-100% saturation and the range for the temperature was from 20-140°C. These tests were conducted for chloride solutions (NaCl, $MgCl_2$, $CaCl_2$, KCl, and NH_4Cl), nitrate solutions (KNO_3 and $NaNO_3$), sulfate solutions ($CaSO_4$ and Na_2SO_4), and solutions representing the stoichiometric dissolution of 304L and 316L SS. These salts were selected because those salts were identified as found on the actual dry storage canisters by Sandia National Laboratories[22]. Stoichiometric solutions simulate pit solutions and were used to calculate the corrosion rate, OCP, and E_{rp} at various levels of saturation.

2.2 MATLAB Software

A MATLAB code was created to calculate the maximum pit size using the framework that was set forth by Chen and Kelly, but has not been published yet[10,15,23]. The tests that were computed include: maximum radius, r_{max}, versus dissolution current/pit radius (I/r), LD, and RH for 304L and 316L SS. The ranges for each of the variables were 0.05 – 0.6 A/m for I/r, 10 – 1,000 ug/cm^2 for LD, and 30 – 98% RH. Temperature plots were made for r_{max} versus LD and RH for 304L and 316L SS at 25°C, 35°C, 45°C, and 55°C.

3. Results

3.1 Computational Results

In this section, the chloride solutions will be presented first, followed by nitrate, sulfate, and stoichiometric solutions respectively. For the chloride, nitrate, and sulfate solutions, the corrosion rates, OCP, and E_{rp} will be shown as a function of the compound concentration and temperature and for stoichiometric solutions, it will be shown at various levels of saturation. Additionally, when a sharp transition can be seen in the graphs, the origins of the corrosion potential effects will be shown with Evans diagrams for conditions just below and just above the sharp transition.

Chloride Solutions

A subset of the data is shown below for these solutions as 316L SS produced the same results as 304L SS did, but on a significantly smaller scale and was therefore not included with the rest of the figures in this section. The figures that are not included in this section can be seen in the Appendix.

NaCl

The results of the chloride effects for NaCl can be seen below in Figure 2. As the concentration of NaCl increases, there is a large effect on the corrosion rate for 304L SS (Fig. 2a) and the repassivation potential decreases for 304L and 316L SS (Fig. 2b). For comparison, Figure 2b also includes experimental results that were found in a recently published paper[15]. The stream amount for Figure 2 was 55.5082 mol.

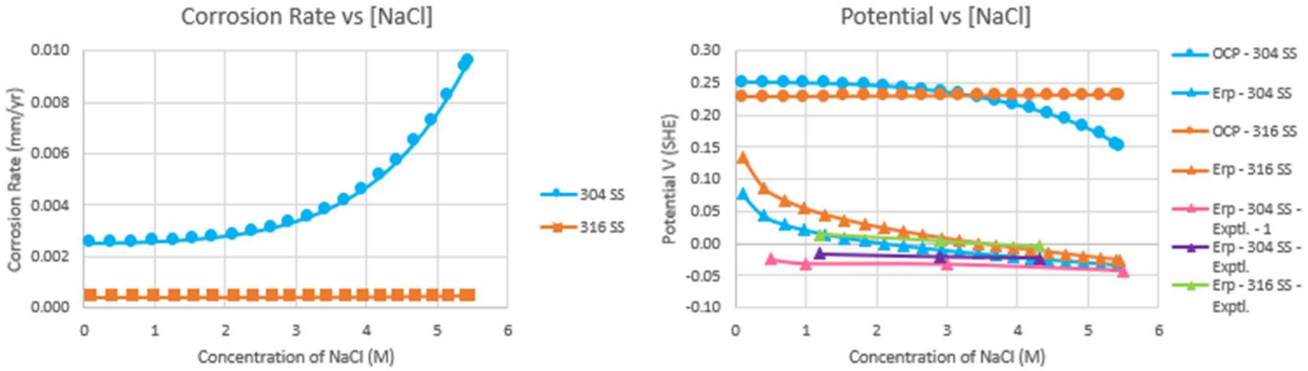

Figure 2: Corrosion rate (a) and potential (E_{rp} and OCP) (b) vs [NaCl][15]

The results of the temperature effects can be seen below in Figure 3. As the temperature increases, the corrosion rate also increases for 304L SS (Fig. 3a). It also increased for 316L SS, but on a significantly smaller scale and was therefore not included with the rest of the figures. As the temperature increases, the OCP decreases for 304L SS with the largest effect at high NaCl concentrations (Fig. 3b). Sharp transitions in the OCP for 304L SS occur at critical temperatures, resulting in the OCP being lower than the E_{rp} (Fig. 3b). In simple salt solutions, 316L SS is more resistant to increased chlorides at increased temperatures than 304L SS, as expected (Fig. 3c). The temperature range only went up to 100°C as the model was not able to determine data past that temperature. At the highest temperatures studied, the OCP for 316L SS shows the beginning of a decrease. The stream amounts for Figure 3 for 0.1 M, 2.1 M, 3.9 M, and 5.4 M were 56.6082 mol, 58.7082 mol, 60.8082 mol, and 62.6582 mol respectively.

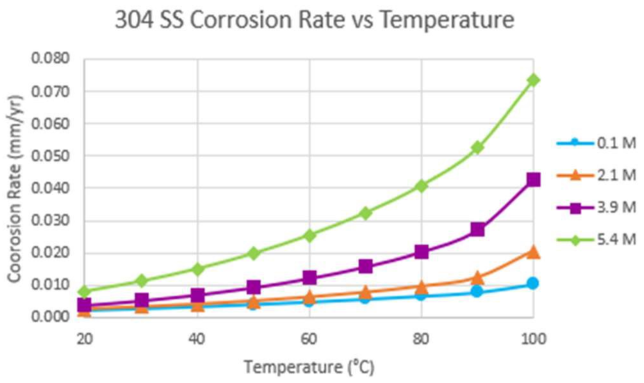

Figure 3a: Corrosion rate of NaCl on 304L SS vs T

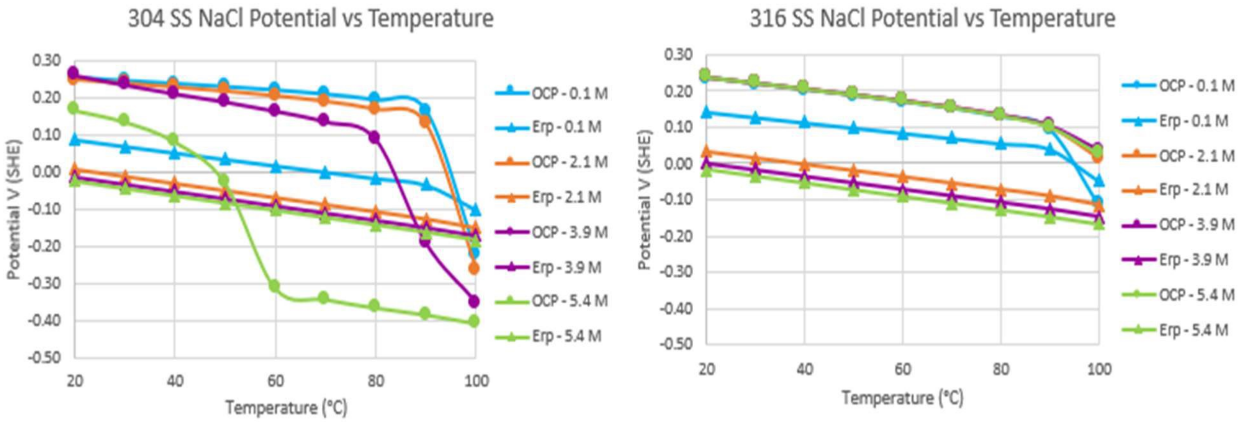

304 SS NaCl Potential vs Temperature

316 SS NaCl Potential vs Temperature

Figure 3 Continued: Potential (E_{rp} and OCP) of NaCl on 304L (b) and 316L SS (c) vs T

The origins of the corrosion potential effects can be seen below in Figure 4 with Evans diagrams from OLI for temperatures just below and just above the sharp transition that was seen in Figure 3b. When there is an increase in passive current density where it exceeds the diffusion-limited oxygen reduction reaction for 304L SS for NaCl, the corrosion potential drops, per Mixed Potential Theory.

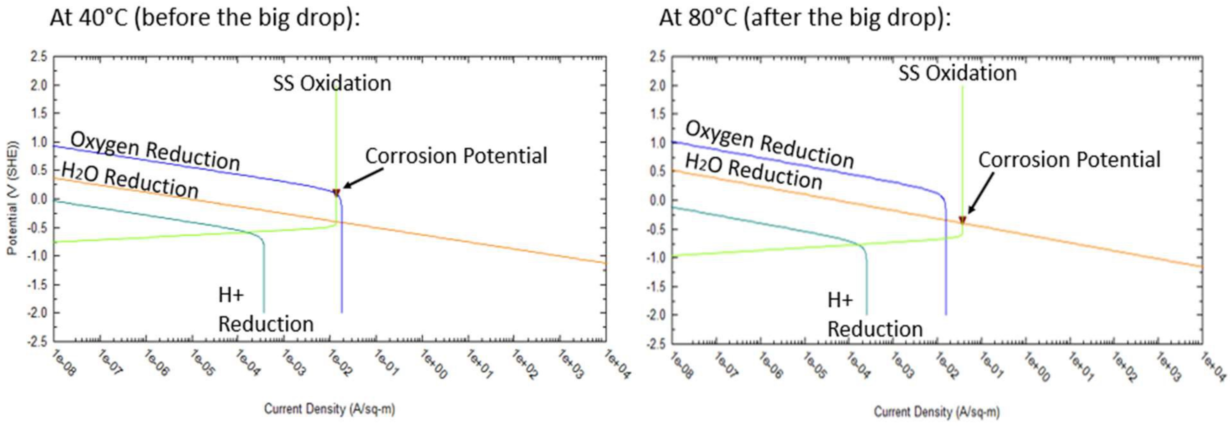

At 40°C (before the big drop):

At 80°C (after the big drop):

Figure 4: Evans diagrams of 5.4 M NaCl on 304L SS at 40°C before (a) and 80°C after (b) sharp transition

$MgCl_2$

The results of the chloride effects for $MgCl_2$ can be seen below in Figure 5. There is a peak in the corrosion rate at ~2 M for 304L SS (Fig. 5a). Above a critical concentration (which is 1.5 M for 304L and 4 M for 316L SS), the corrosion potential falls below the repassivation potential (Fig. 5b). The stream amount for Figure 5 was 55.5082 mol.

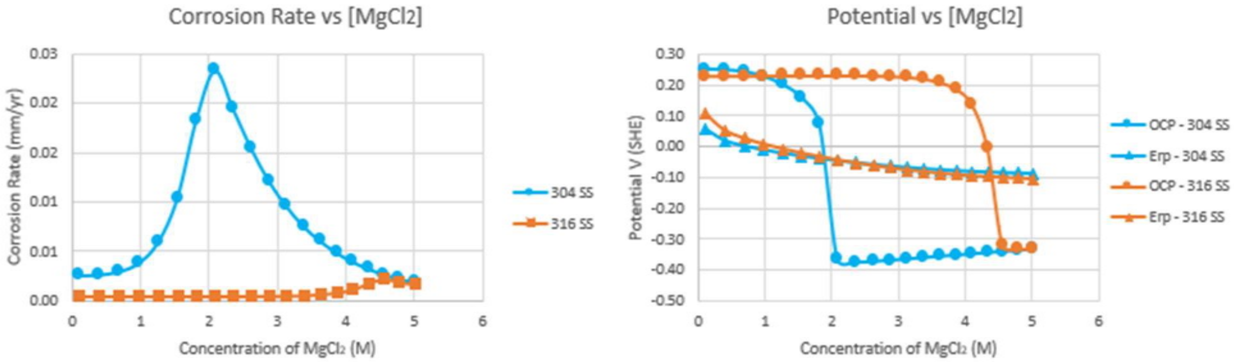

Figure 5: Corrosion rate (a) and potential (E_{rp} and OCP) (b) vs [$MgCl_2$]

The origins of the corrosion potential effects can be seen below in Figure 6 with Evans diagrams of before, at, and after the peak that was seen in Figure 5a. It can be seen that the corrosion potential drops and the anodic current density increases from 1 M to 2 M for 304L SS.

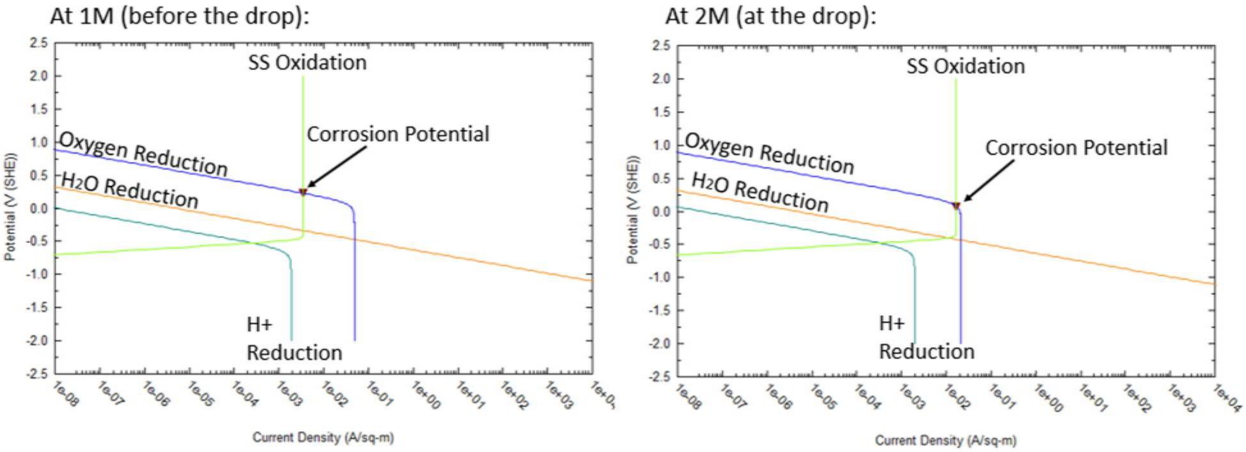

Figure 6: Evans diagrams of 1 M (a) and 2 M (b) $MgCl_2$ on 304L SS

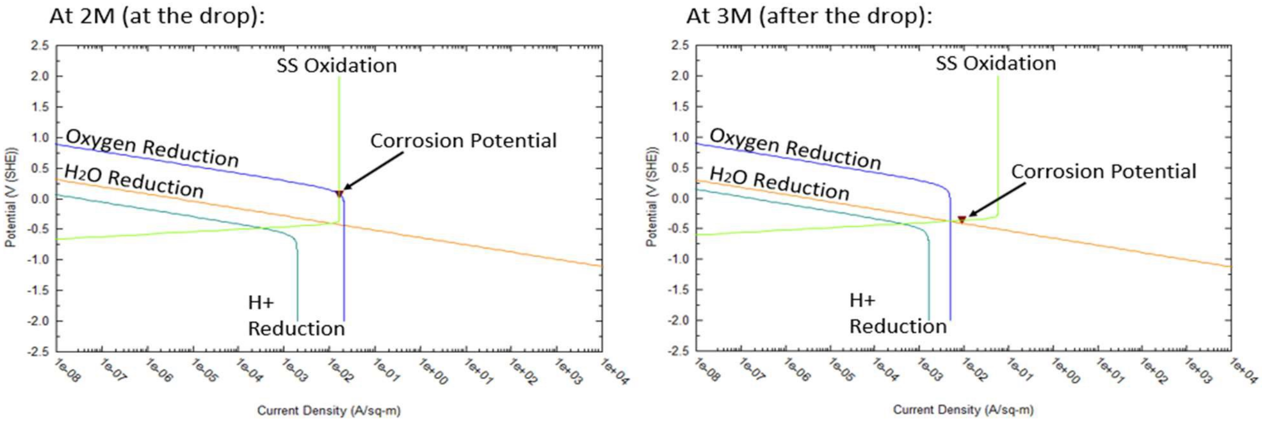

Figure 6 Continued: Evans diagrams of 2 M (b) and 3 M (c) $MgCl_2$ on 304L SS

The results of the temperature effects on corrosion rate can be seen below in Figure 7. Increased temperature leads to switching the order of magnitude for different concentrations of $MgCl_2$ (Fig. 7a). When the OCP falls below the E_{rp} with increased temperature, the critical temperature is lower for higher concentration (Fig. 7b). For 5 M of $MgCl_2$ for 304L SS, the OCP is always less than the E_{rp} (Fig. 7b). 316L SS produced the same results as 304L SS did, but on a significantly smaller scale and was therefore not included with the rest of the figures. Figure 8 displays Evans diagrams of before and after the sharp transition that was seen in Figure 7b. The stream amounts for Figure 7 for 0.1 M, 1.8 M, 3.4 M, and 5.0 M were 56.6082 mol, 58.4082 mol, 60.2082 mol, and 62.3082 mol respectively.

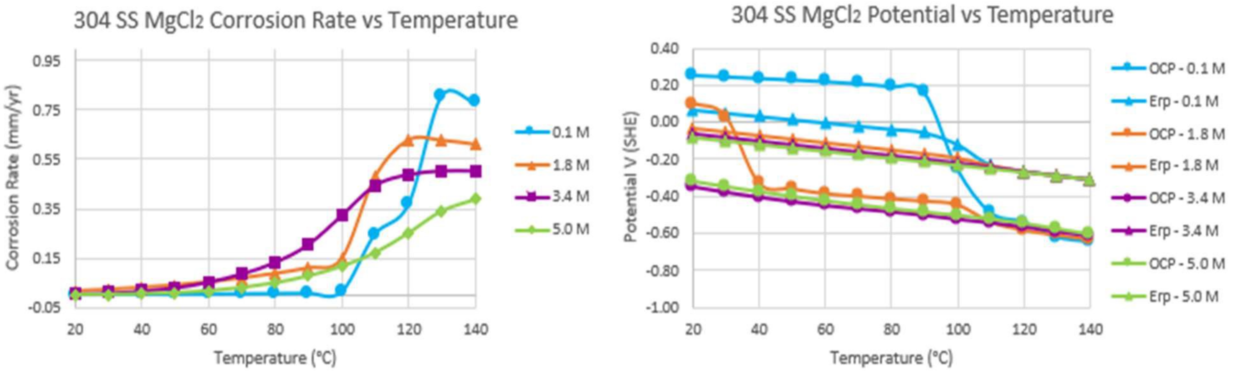

Figure 7: Corrosion rate (a) and potential (E_{rp} and OCP) (b) of $MgCl_2$ on 304L SS vs T

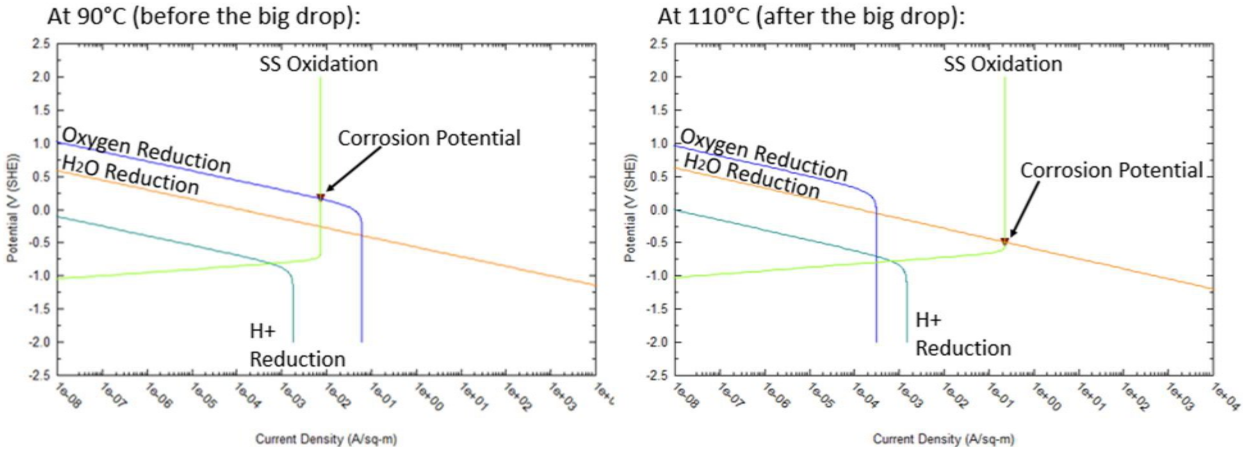

Figure 8: Evans diagrams of 0.1 M $MgCl_2$ on 304L SS at 90°C before (a) and 110°C after (b) sharp transition

$CaCl_2$

The results of the chloride effects for $CaCl_2$ are shown below in Figure 9. The results of $CaCl_2$ are qualitatively the same to the results of $MgCl_2$. There is a peak in the corrosion rate at ~2.65 M for 304L SS (Fig. 9a). Above critical concentration (which is 1.5 M for 304L and 4 M for 316L SS), the OCP will fall below the E_{rp} (Fig. 9b). The stream amount for Figure 9 was 56.5082 mol.

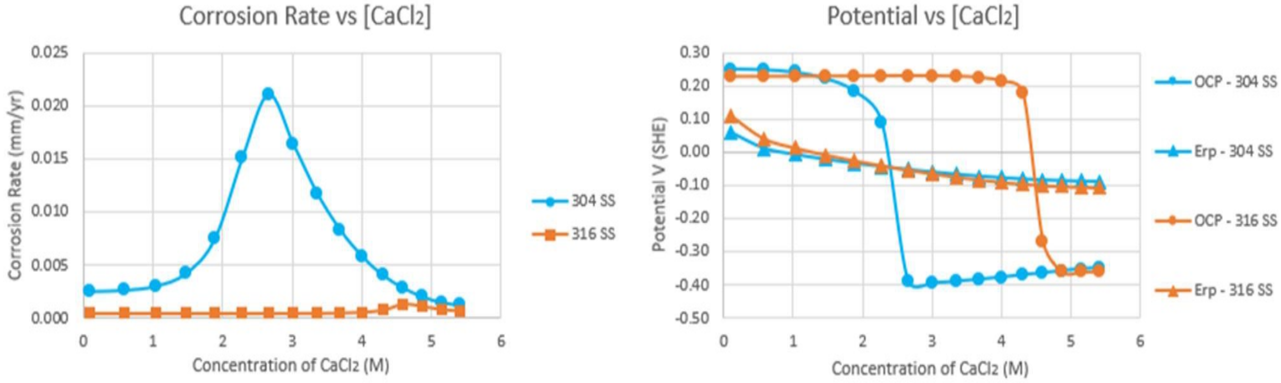

Figure 9: Corrosion rate (a) and potential (E_{rp} and OCP) (b) vs [$CaCl_2$]

The origins of the corrosion potential effects are shown below in Figure 10 with Evans diagrams of before, at, and after the peak that was seen in Figure 9a. It can be seen that the corrosion potential drops when the anodic current density increases from 1 M to 2.65 M (Figs. 10a,b). The corrosion potential stays the same and the anodic current density decreases from 2.65 M to 4 M for 304L SS (Figs. 10b,c).

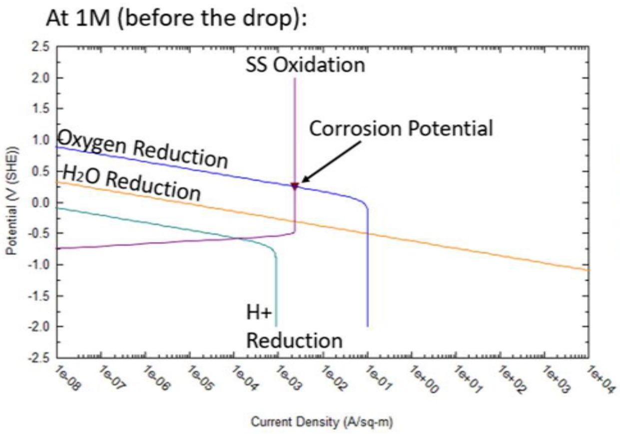

Figure 10: Evans diagrams of 1 M (a) and 2.65 M (b) $CaCl_2$ on 304L SS

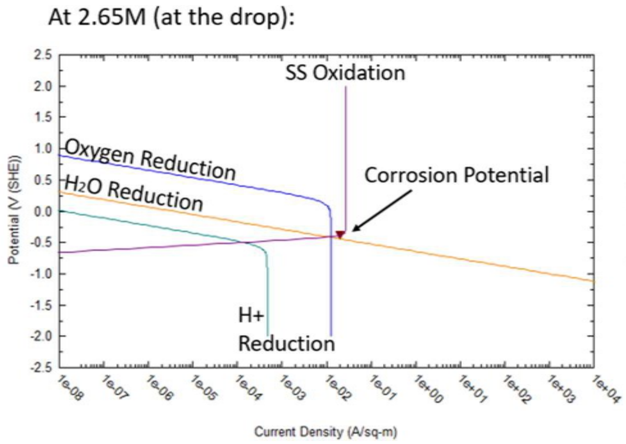

Figure 10 Continued: Evans diagrams of 2.65 M (b) and 4 M (c) $CaCl_2$ on 304L SS

The results of the temperature effects can be seen below in Figure 11. Increased temperature leads to switching the order of magnitude for different concentrations of $CaCl_2$ (Fig.

11a). When the OCP falls below the E_{rp} with increased temperature, the critical temperature is lower for higher concentration of $CaCl_2$ (Fig. 11b). For 5 M of $CaCl_2$ on 304L SS, the OCP is always less than the E_{rp} (Fig. 11b). 316L SS produced the same results as 304L SS did, but on a significantly smaller scale and was therefore not included with the rest of the figures. Figure 12 displays Evans diagrams of before and after the sharp transition that was seen in Figure 11b. The stream amounts for Figure 11 for 0.1 M, 2.3 M, 4.0M, and 5.4 M were 56.6082 mol, 59.1082 mol, 61.6082 mol, and 63.9582 mol respectively.

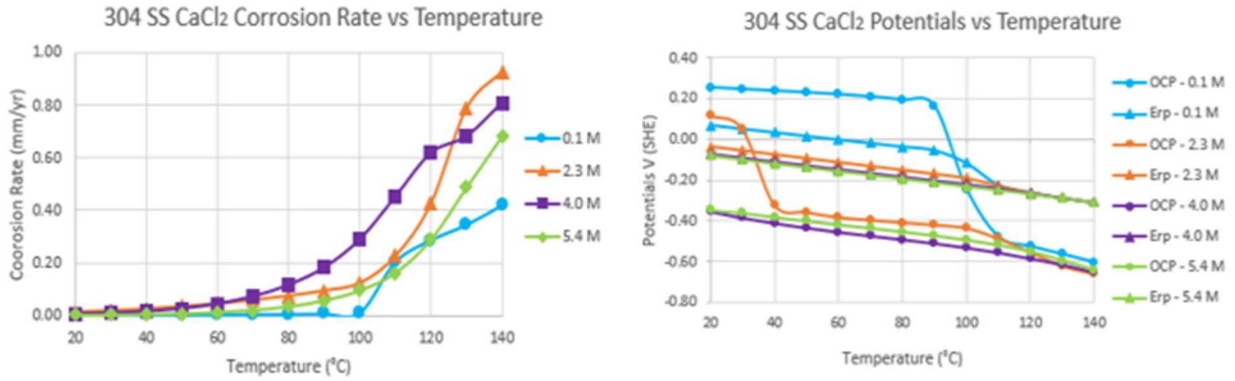

Figure 11: Corrosion rate (a) and potential (OCP and E_{rp}) (b) of $CaCl_2$ on 304L SS vs T

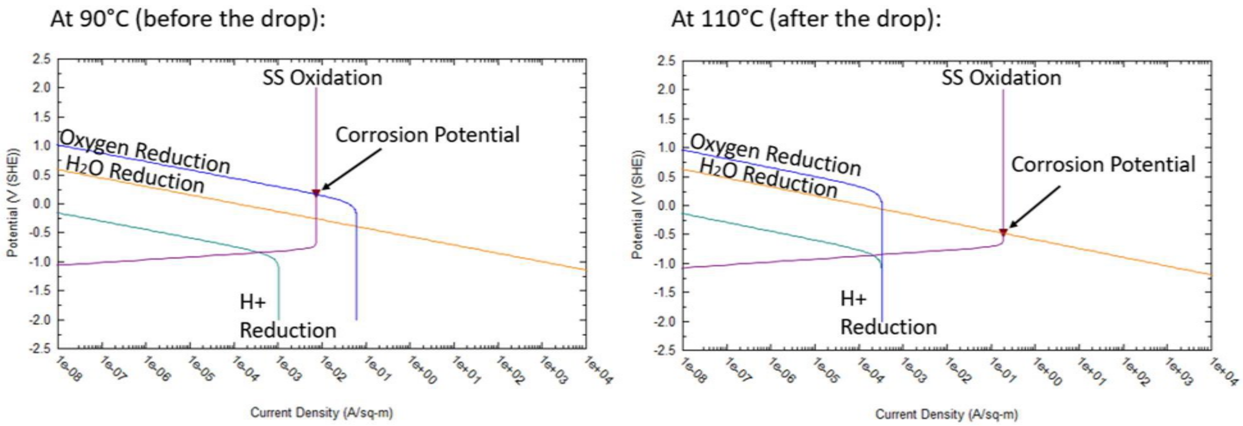

Figure 12: Evans diagrams of 0.1 M $CaCl_2$ on 304L SS at 90°C before (a) and 110°C after (b) sharp transition

KCl

The results of the chloride effects for KCl can be seen below in Figure 13. As the concentration of KCl increases, the corrosion rate increases for 304L SS (Fig. 13a) whereas the OCP and E_{rp} slightly decrease for both alloys (Fig. 13b). The stream amount for Figure 13 was 56.5082 mol.

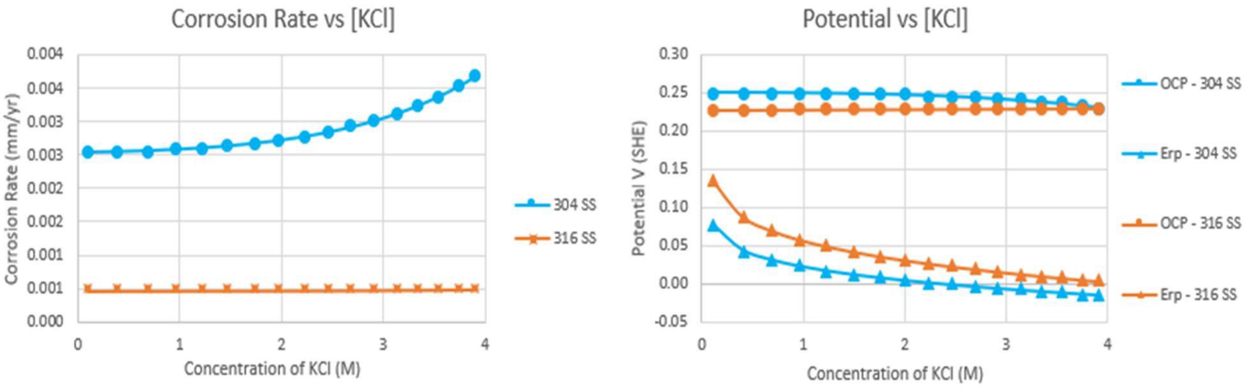

Figure 13: Corrosion rate (a) and potential (E_{rp} and OCP) (b) vs [KCl]

The results of the temperature effects can be seen below in Figure 14. There is a peak in the corrosion rate at 100°C for 304L SS (Fig. 14a). Sharp transitions in the OCP for 304L SS occur at critical temperature where the OCP is lower than the E_{rp} (Fig. 14b). 316L SS produced the same results as 304L SS did, but on a significantly smaller scale and was therefore not included with the rest of the figures. The temperature range only went up to 130°C as the model could not determine data past that temperature. The stream amounts for Figure 14 for 0.1 M, 1.5 M, 2.7 M, and 3.9 M were 56.6082 mol, 58.1082 mol, 59.6082 mol, and 61.3282 mol respectively.

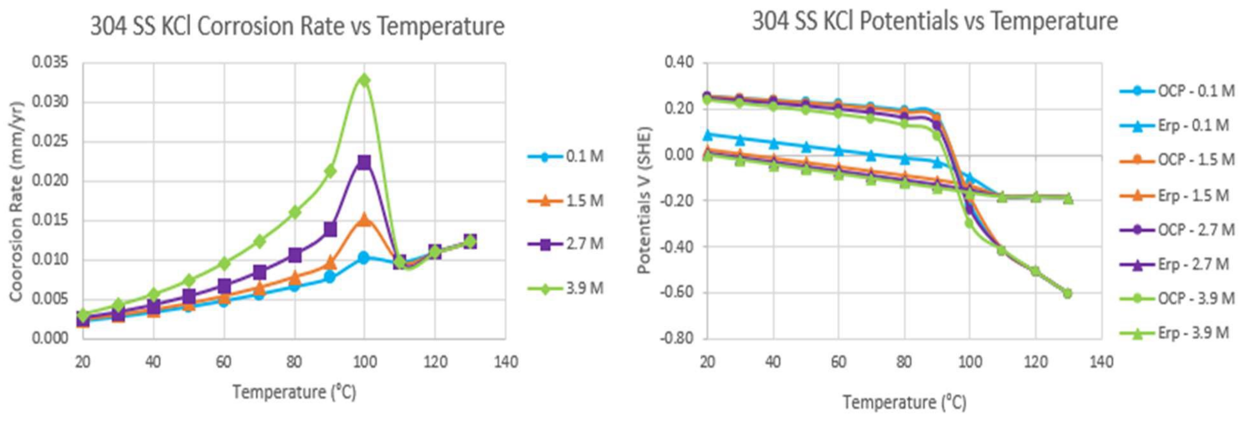

Figure 14: Corrosion rate (a) and potential (E_{rp} and OCP) (b) of KCl on 304L SS vs T

The origins of the corrosion potential effects are shown below in Figures 15 and 16 with Evans diagrams of before, at, and after the peak seen in Figure 13a and before and after the sharp transition seen in Figure 14b. Figure 15a,b shows that the corrosion potential drops and anodic current density increases from 80-100°C for 3.9 M KCl on 304L SS. Figure 15b,c shows that the corrosion potential slightly drops and anodic current density slightly decreases from 100-110°C for 3.9 M KCl on 304L SS. Similar to Figure 15, Figure 16a,b shows that the corrosion potential drops and anodic current density increases from 90-110°C for 0.1 M KCl on 304L SS.

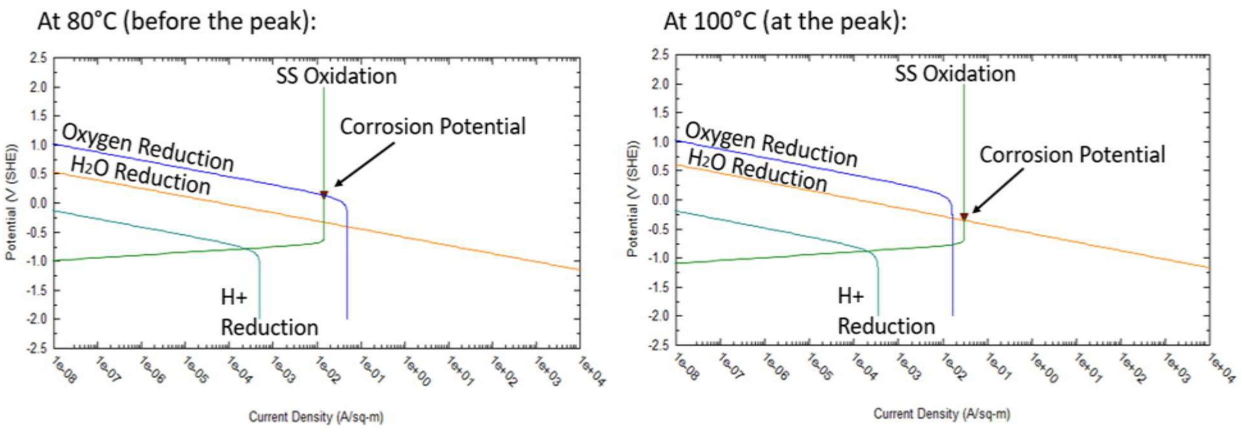

Figure 15: Evans diagrams of 3.9 M KCl on 304L SS at 80°C before (a) and 100°C (b) sharp transition

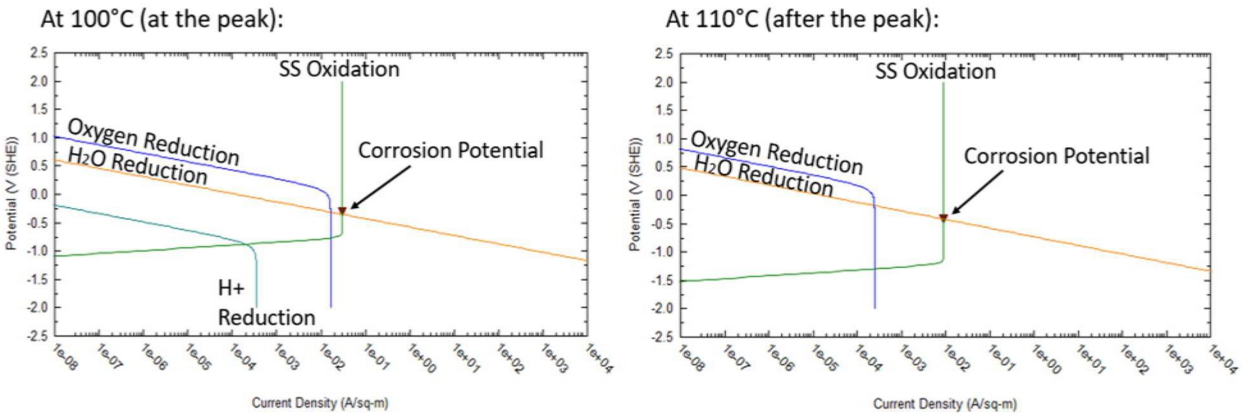

Figure 15 Continued: Evans diagrams of 3.9 M KCl on 304L SS at 100°C (b) and 110°C after (c) sharp transition

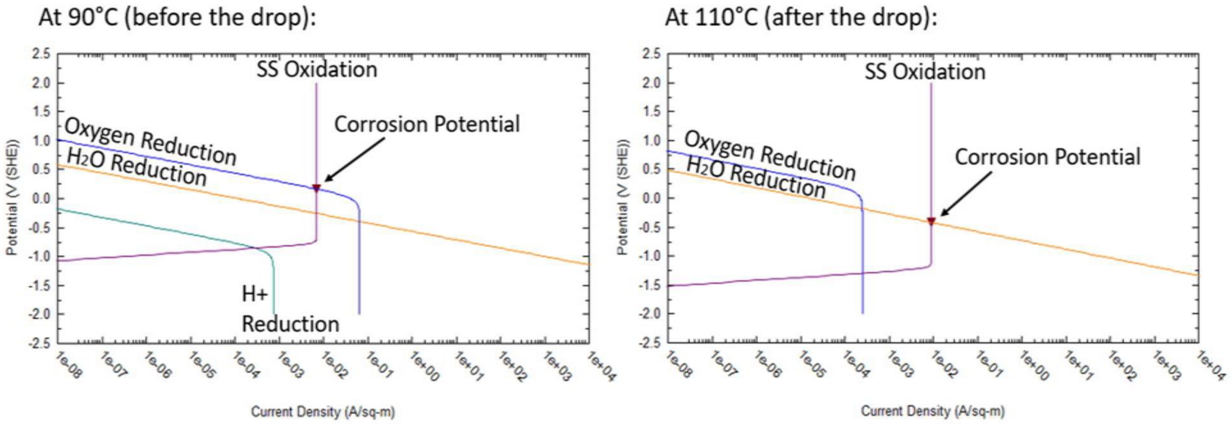

Figure 16: Evans diagrams of 0.1 M KCl on 304L SS at 90°C before (a) and 110°C after (b) sharp transition

NH_4Cl

The results of the chloride effects for NH_4Cl can be seen below in Figure 17. As the concentration of NH_4Cl increases, the corrosion rate increases for 304L SS (Fig. 17a), the corrosion potential decreases for 304L SS (Fig. 17b), and the repassivation potential decreases for both alloys (Fig. 17b). The stream amount for Figure 17 was 56.5082 mol.

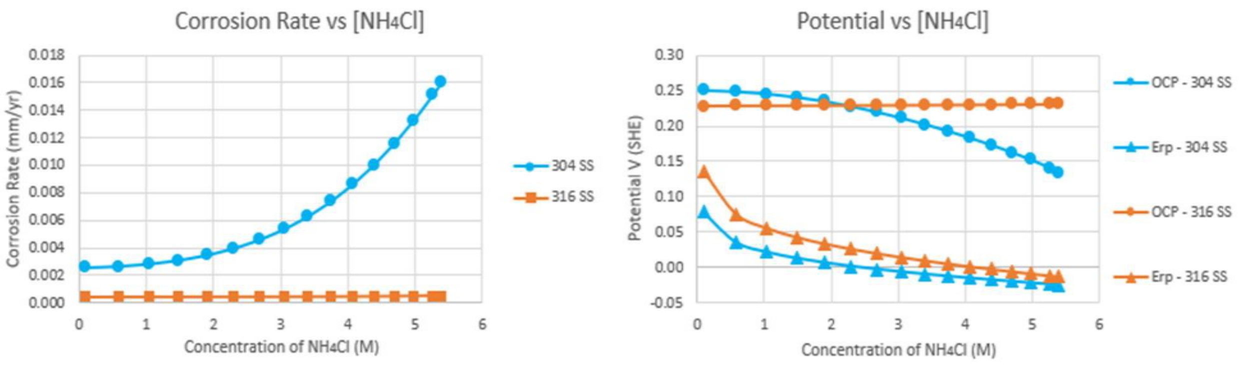

Figure 17: Corrosion rate (a) and potential (E_{rp} and OCP) (b) vs [NH_4Cl]

The results of the temperature effects for NH_4Cl can be seen below in Figure 18. There is a peak in the corrosion rate at 100°C for 304L SS (Fig. 18a). Sharp transitions in the OCP for 304L SS occur at critical temperature where the corrosion potential is lower than the E_{rp} (Fig. 18b). 316L SS produced the same results as 304L SS did, but on a significantly smaller scale and was therefore not included with the rest of the figures. The temperature range only went up to 130°C as the model was not able to determine data past that temperature. The stream amounts for Figure 18 for 0.1 M, 2.3 M, 4.1 M, and 5.4 M were 56.6082 mol, 59.1082 mol, 61.6082 mol, and 63.8582 mol respectively.

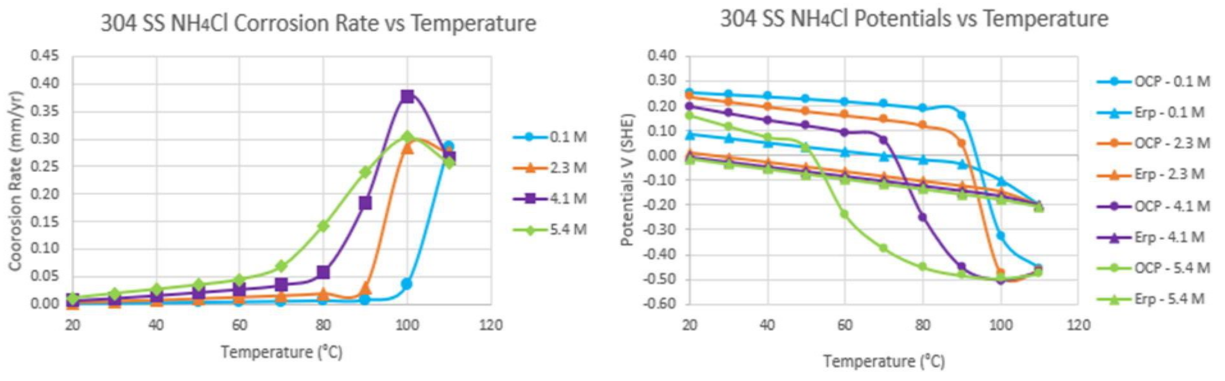

Figure 18: Corrosion rate (a) and potential (E_{rp} and OCP) (b) of NH_4Cl on 304L SS vs T

The origins of the corrosion potential effects can be seen below in Figures 19 and 20 with Evans diagrams of before, at, and after the sharp transition that was seen in Figure 18a and before and after the sharp transition in Figure 18b. Figure 19a,b shows that the corrosion potential drops and the anodic current density increases from 80-100°C for 4.1 M NH_4Cl on 304L SS. Figure 19b,c shows that the corrosion potential slightly increases and the anodic current density increases from 100-110°C for 4.1 M NH_4Cl on 304L SS. Figure 20 shows that the corrosion potential drops and the anodic current density increases from 80-100°C for 0.1 M NH_4Cl on 304L SS.

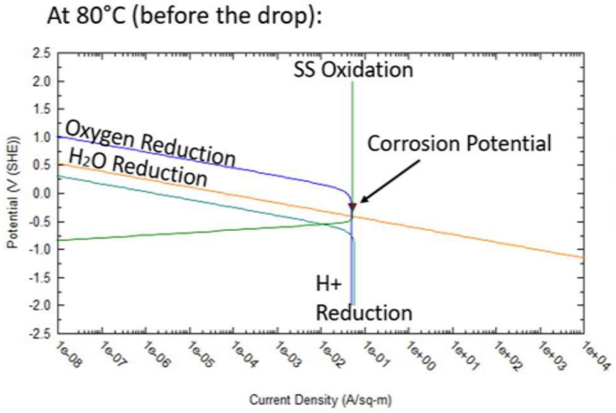

Figure 19: Evans diagrams of 4.1 M NH_4Cl on 304L SS at 80°C before (a) and 100°C at (b) sharp transition

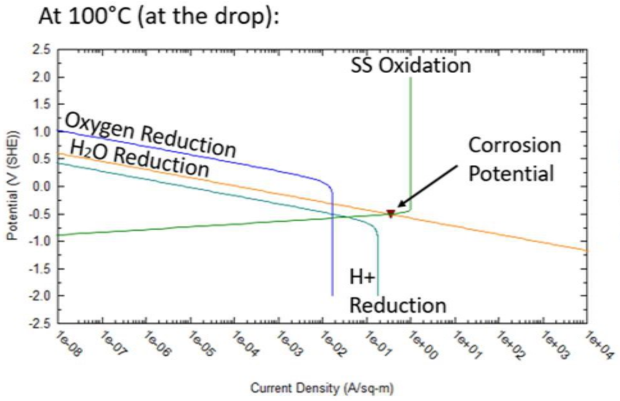

Figure 19 Continued: Evans diagrams of 4.1 M NH_4Cl on 304L SS at 100°C (b) and 110°C after (c) sharp transition

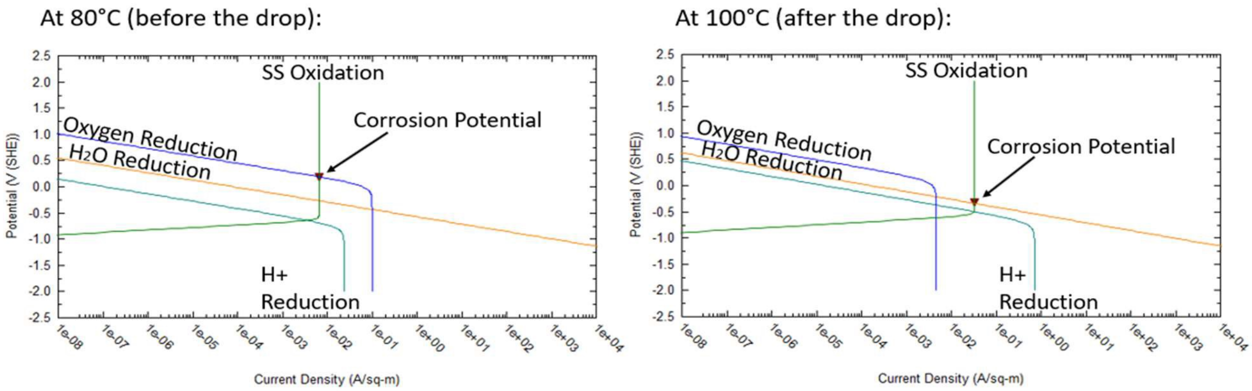

Figure 20: Evans diagrams of 0.1 M NH_4Cl on 304L SS at 80°C before (a) and 100°C after (b) sharp transition

Nitrate Solutions

Since the nitrate solutions do not contain any aggressive anions, (e.g., chlorides), that can advance the localized corrosion development, no localized corrosion of SS was found which resulted in no repassivation potential.

KNO_3

The results of the concentration effects for KNO_3 can be seen below in Figure 21. As the concentration of KNO_3 increases, the corrosion rate slightly decreases for 304L SS (Fig. 21a) whereas the corrosion potential slightly increases for both alloys (Fig. 21b). The stream amount for Figure 21 was 56.5082 mol.

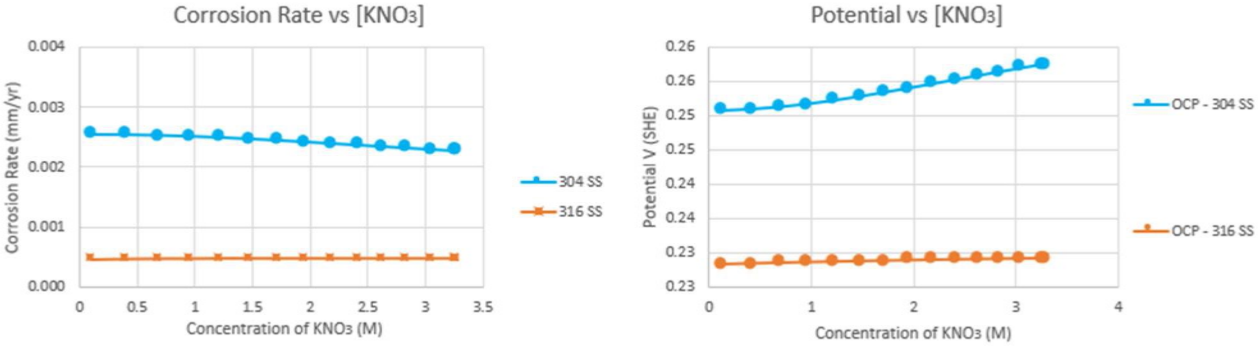

Figure 21: Corrosion rate (a) and OCP (b) vs [KNO_3]

The results of the temperature effects can be seen below in Figures 22 and 23. As the temperature increases, the corrosion rate for KNO_3 increases for both alloys (Fig. 22a,b). Sharp transitions in the corrosion potential for both alloys occur (Fig. 23). The stream amounts for Figures 22 and 23 for 0.1 M, 1.5 M, 2.4 M, and 3.3 M were 56.6082 mol, 58.1082 mol, 59.3082 mol, and 60.5482 mol respectively.

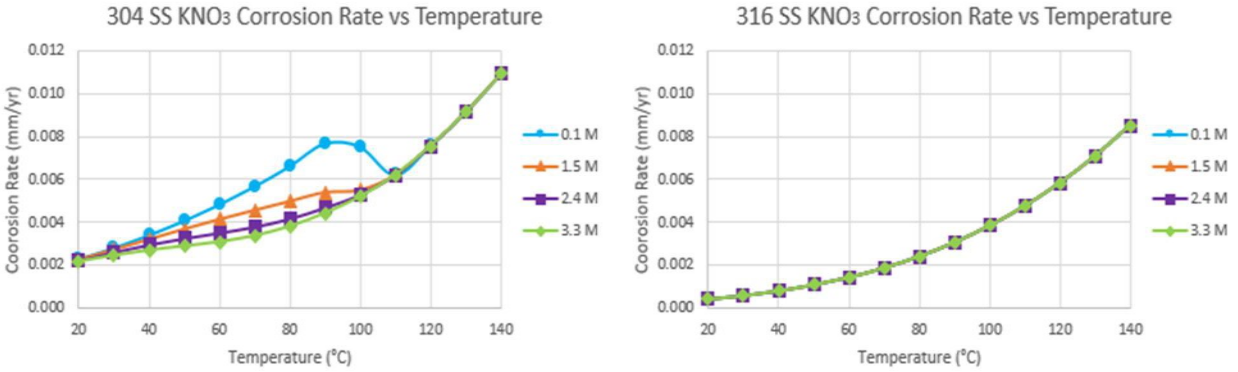

Figure 22: Corrosion rate of KNO_3 on 304L (a) and 316L SS (b) vs T

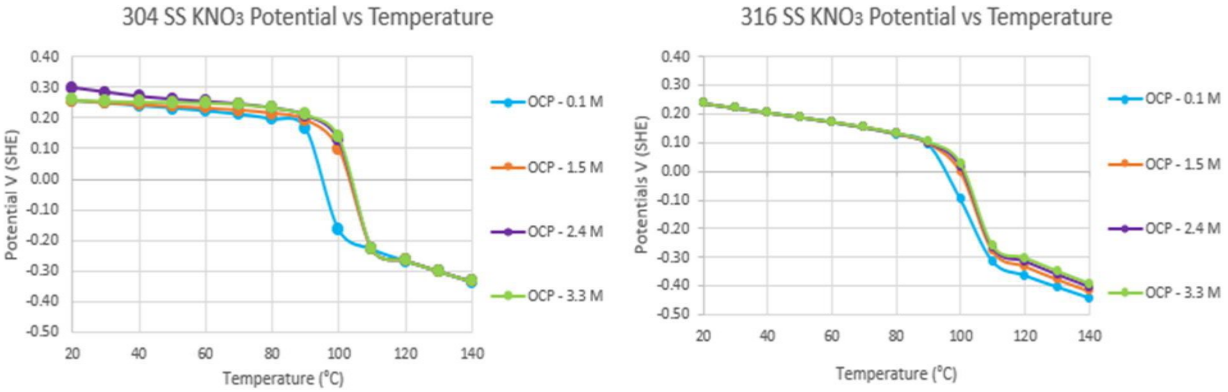

Figure 23: OCP of KNO_3 on 304L (a) and 316L SS (b) vs T

The origins of the corrosion potential effects can be seen below in Figure 24 with Evans diagrams of before and after the sharp transition that was seen in Figure 23. Figure 24 shows that the corrosion potential drops and the anodic current density increases from 90-110°C for 0.1 M KNO_3 on 304L SS.

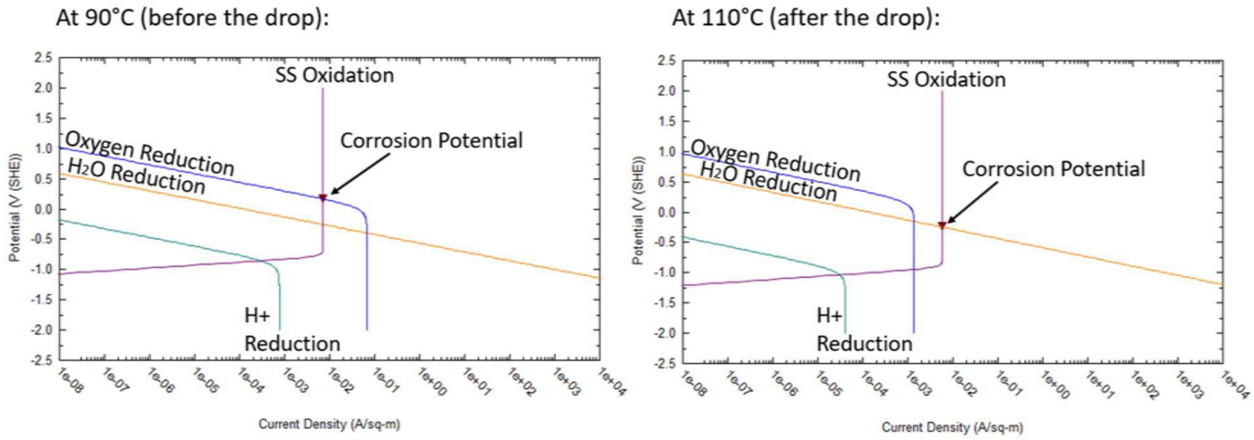

Figure 24: Evans diagrams of 0.1 M KNO_3 on 304L SS at 90°C before (a) and 110°C after (b) sharp transition

$NaNO_3$

The results of the concentration effects for $NaNO_3$ can be seen below in Figure 25. As the concentration of $NaNO_3$ increases, the corrosion rate decreases for 304L SS (Figure 25a) and the corrosion potential for both alloys increase to a certain point and then drops off (Fig. 25b). The stream amount for Figure 25 was 56.5082 mol.

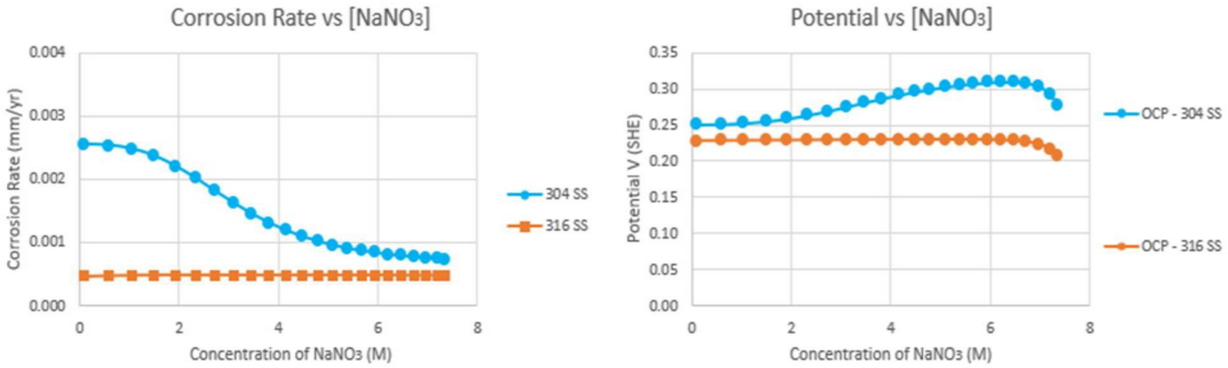

Figure 25: Corrosion rate (a) and OCP (b) vs [$NaNO_3$]

The results of the temperature effects can be seen below in Figures 26 and 27. As the temperature increases, the corrosion rate also increases for both alloys (Fig. 26) and sharp transitions in the corrosion potential for 304L SS occur (Fig. 27). The temperature range only went up to 120°C as the model could not determine data past that temperature. The stream amounts for Figures 26 and 27 for 0.1 M, 3.5 M, 5.7 M, and 7.4 M were 56.6082 mol, 60.6082 mol, 64.1082 mol, and 67.4582 mol respectively.

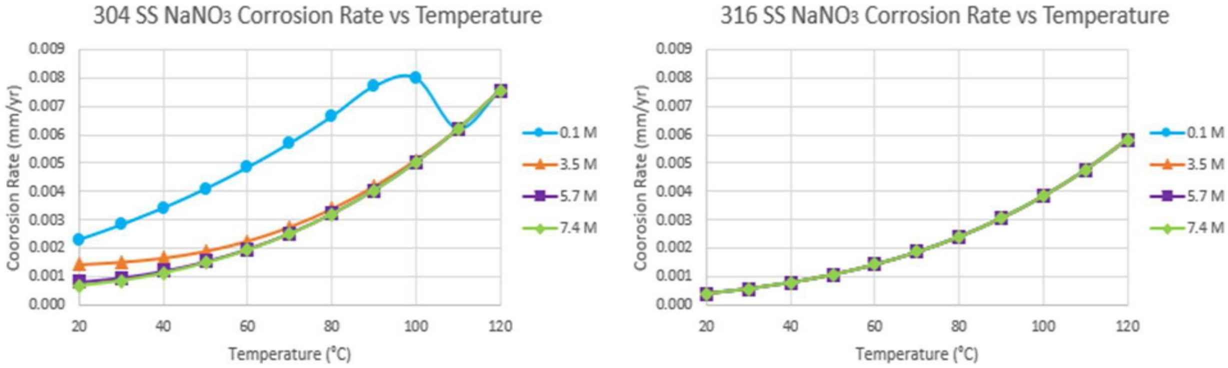

Figure 26: Corrosion rate of $NaNO_3$ on 304L (a) and 316L SS (b) vs T

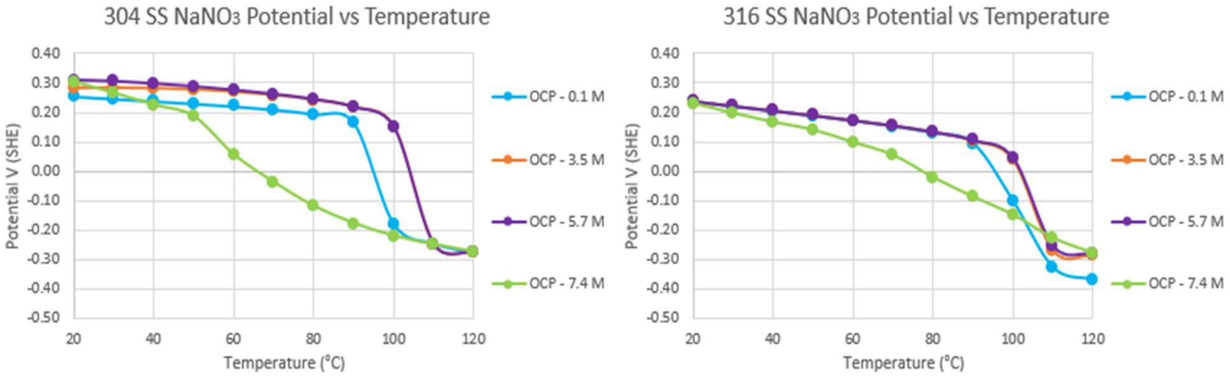

Figure 27: OCP of $NaNO_3$ on 304L (a) and 316L SS (b) vs T

The origins of the corrosion potential effects can be seen below in Figure 28 with Evans diagrams of before and after the sharp transition that was seen in Figure 27. As the temperature increases from 90-110°C, the corrosion potential drops and the anodic current density increases for 0.1 M $NaNO_3$ on 304L SS.

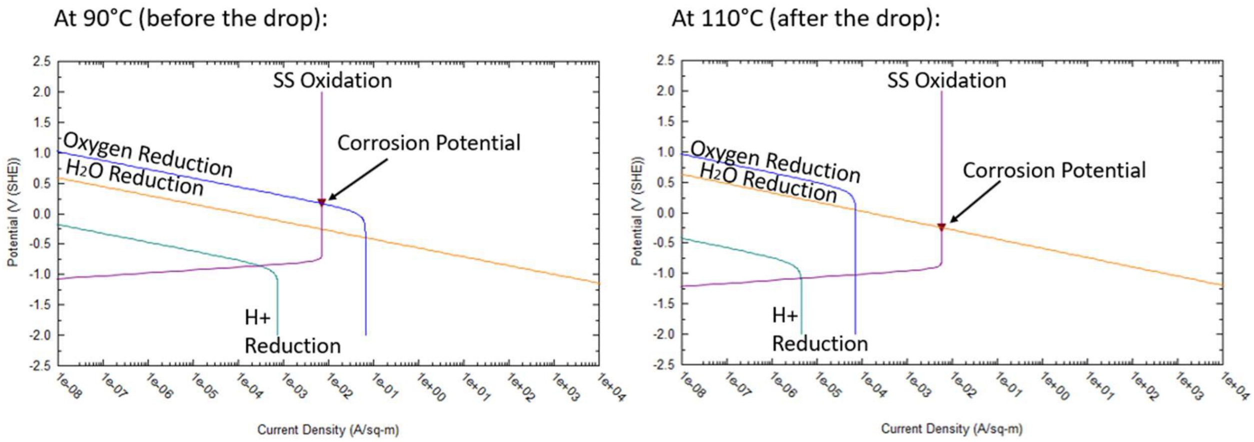

Figure 28: Evans diagrams of 0.1 M $NaNO_3$ on 304L SS at 90°C before (a) and 110°C after (b) sharp transition

Sulfate Solutions

Similar to the nitrate solutions, the sulfate solutions showed no repassivation potential.

$CaSO_4$

The results of the concentration effects for $CaSO_4$ can be seen below in Figure 29. As the concentration increases, the corrosion rate and the OCP stay the same for both alloys. The stream amount for Figure 29 was 56.5082 mol.

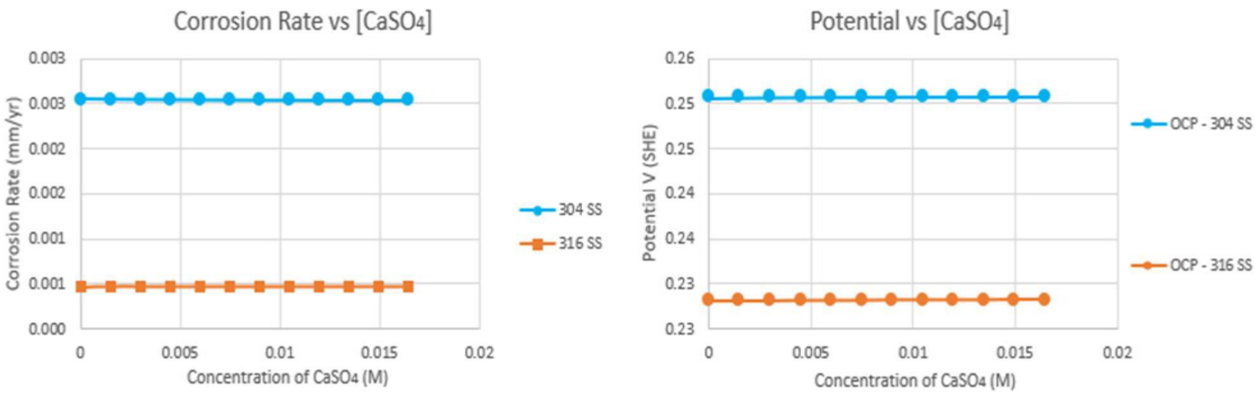

Figure 29: Corrosion rate on 304L (a) and 316L SS (b) vs [$CaSO_4$]

The results of the temperature effects can be seen below in Figures 30 and 31. As the temperature increases, the corrosion rate increases for both alloys (Fig. 30) and the OCP decreases for both alloys (Fig. 31). There was no Evans diagram for $CaSO_4$ as the results did not show any sharp transition as the other compounds did. The temperature range only went up to 90°C as the model could not determine data past that temperature. The stream amounts for Figures 30 and 31 for 0.0015 M, 0.006 M, 0.0105 M, and 0.0165M were 56.5097 mol, 56.5142 mol, 56.5187 mol, and 56.5247 mol respectively.

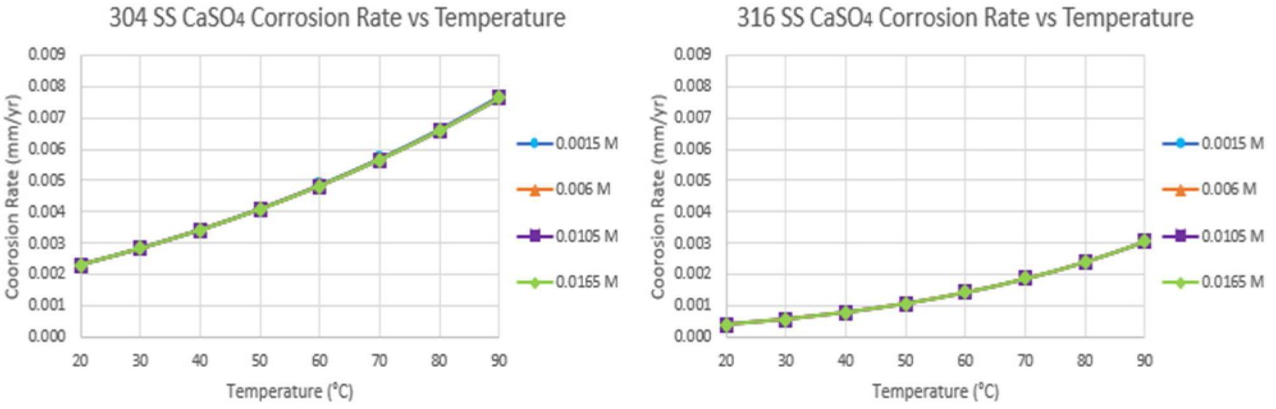

Figure 30: Corrosion rate of $CaSO_4$ on 304L (a) and 316L SS (b) vs T

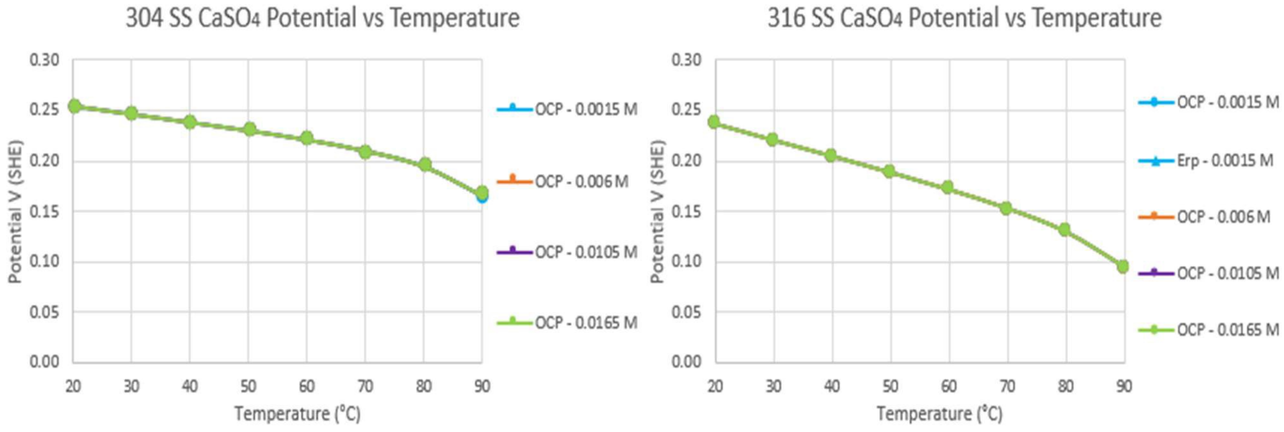

Figure 31: OCP of $CaSO_4$ on 304L (a) and 316L SS (b) vs T

Na_2SO_4

The results of the concentration effects for Na_2SO_4 can be seen below in Figure 32. Similar to $CaSO_4$, as the concentration increases, the corrosion rate and the OCP stay the same. The stream amount for Figure 32 was 56.5082 mol.

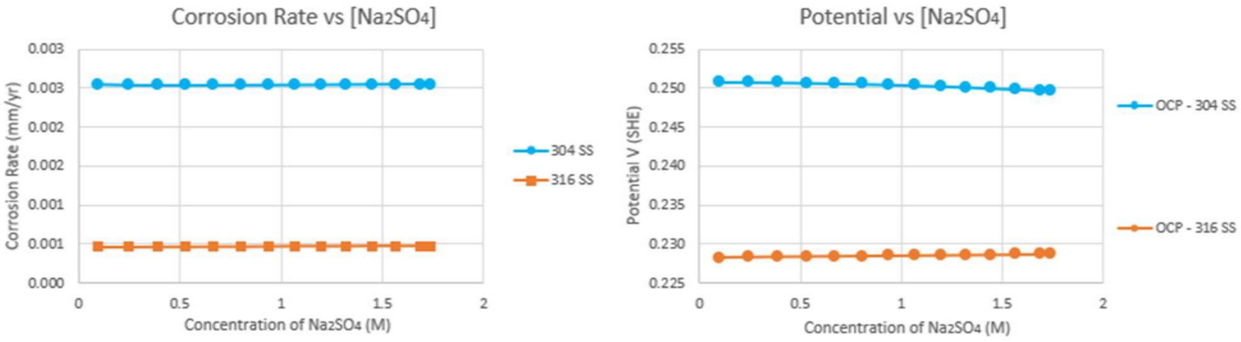

Figure 32: Corrosion rate (a) and OCP (b) vs [Na_2SO_4]

The results of the temperature effects can be seen below in Figures 33 and 34. As the temperature increases, the corrosion rate also increases for both alloys (Fig. 33). Sharp transitions in the corrosion potential for 304L SS occur (Fig. 34). The temperature range only went up to 100°C as the model could not determine data past that temperature. The stream amounts for Figures 33 and 34 for 0.1 M, 0.7 M, 1.3 M, and 1.7 M were 56.5097 mol, 57.2082 mol, 57.9582 mol, and 58.4682 mol respectively.

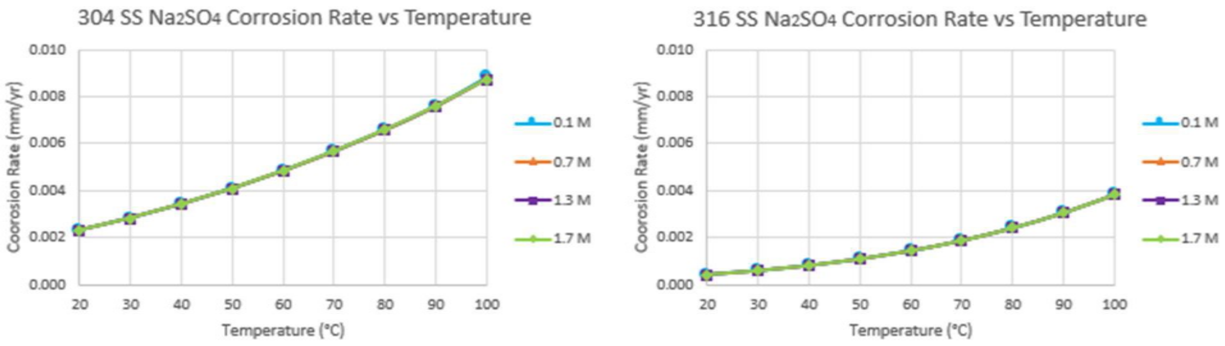

Figure 33: Corrosion rate of Na_2SO_4 on 304L (a) and 316L SS (b) vs T

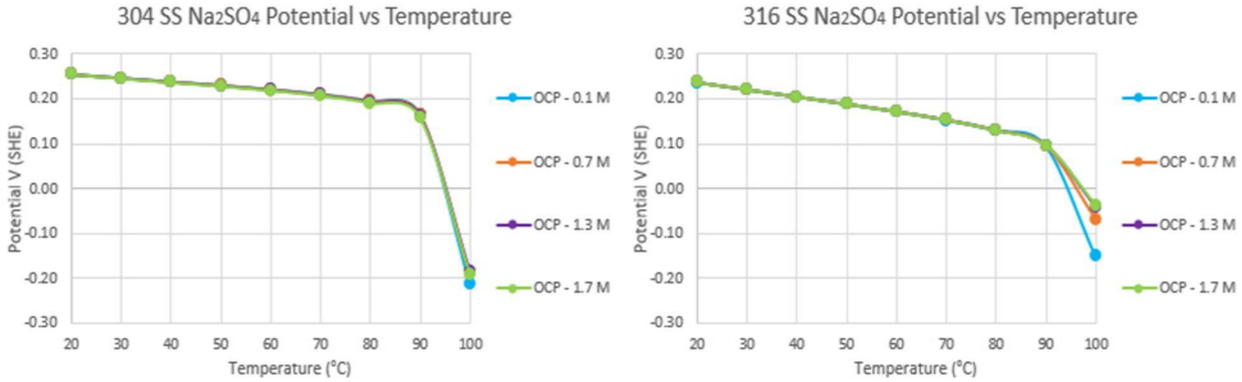

Figure 34: OCP of Na_2SO_4 on 304L (a) and 316L SS (b) vs T

The origins of the corrosion potential effects can be seen below in Figure 35 with Evans diagrams of before and after the sharp transition that was seen in Figure 34. The corrosion potential drops and anodic current density increases from 80-100°C for 0.1 M Na_2SO_4 on 304L.

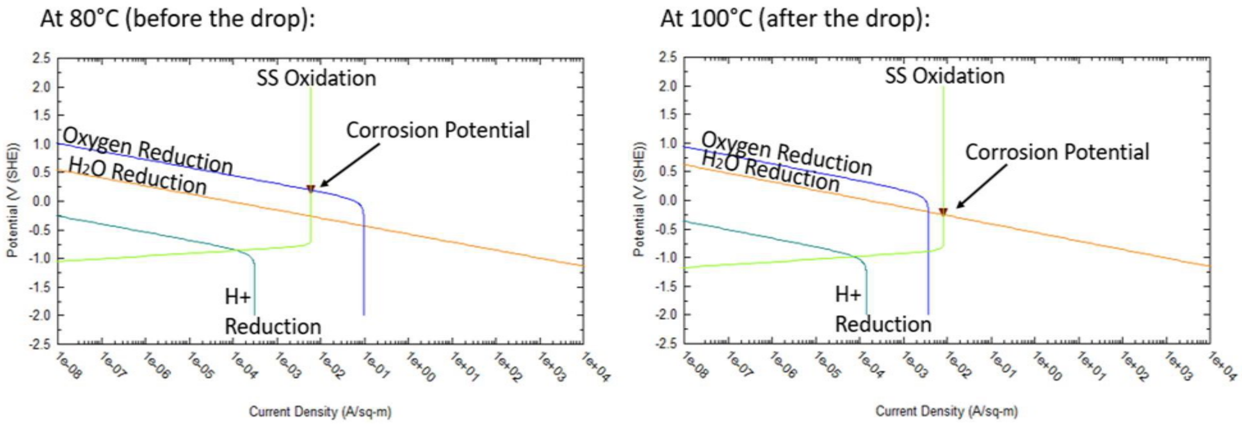

Figure 35: Evans diagrams of 0.1 M Na_2SO_4 on 304L SS at 90°C before (a) and 110°C after (b) sharp transition

Stoichiometric Solutions

The effects of the degree of saturation for a stoichiometric solution on the corrosion rate, OCP (Fig. 36), and Evans diagrams (Fig. 37) can be seen below. Figure 36 shows that the OCP of 304L and 316L SS are below the E_{rp}. Figure 37 shows Evans diagrams at the peak (70% saturation) that can be seen in Figure 36a. The corrosion potential of 304L SS (Fig. 37a) is lower than that of 316L SS (Fig. 37b). The stream amount for Figure 36 for 304L SS was 58.2632 mol and for 316L SS, it was 58.5193 mol.

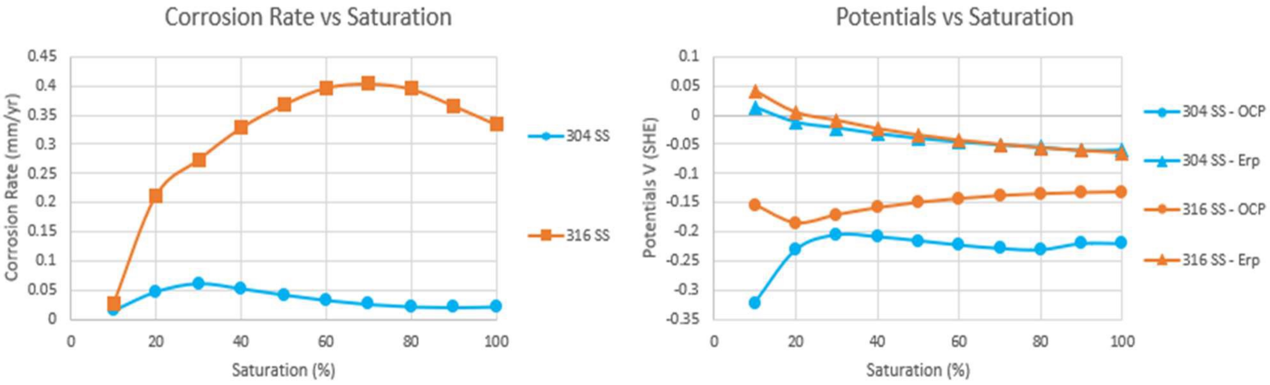

Figure 36: Corrosion rate (a) and potential (E_{rp} and OCP) (b) vs saturation

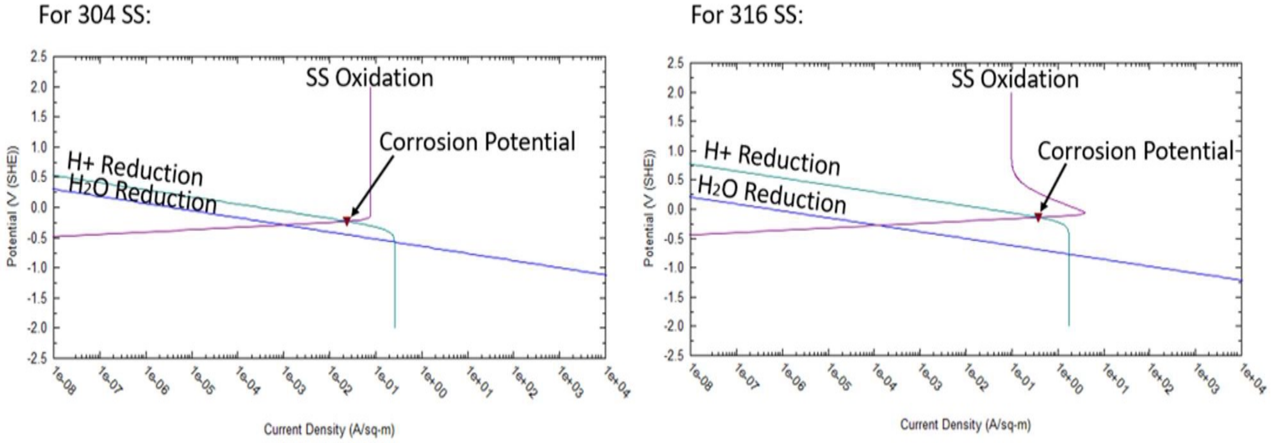

Figure 37: Evans diagrams of 70% saturation on 304L (a) and 316L SS (b)

3.2 Maximum Pit Calculations

The results of r_{max} versus I/r for 304L and 316L SS is shown below in Figure 38. For these results, the temperature was held constant at 25°C, Cl at 0.6 M, RH at 98%, and LD at 0.5 g/m^2. This figure shows that r_{max} and I/r have a negative exponential relationship in both materials.

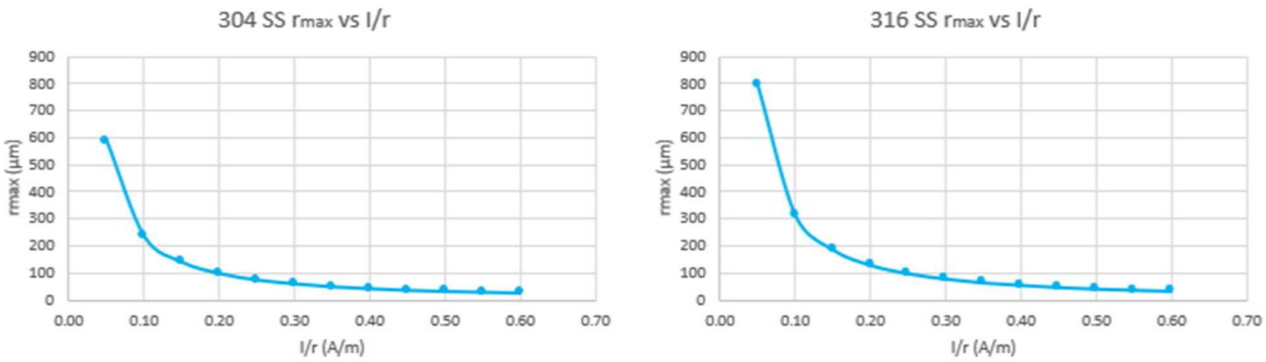

Figure 38: r_{max} vs I/r for 304L (a) and 316L SS (b)

The results of r_{max} versus LD for 304L and 316L SS is shown below in Figure 39. For these results, the temperature was held constant at 25°C, Cl at 0.6 M, RH at 98%, and I/r at 0.844 A/m. This figure shows that r_{max} has a direct relationship with LD in both materials.

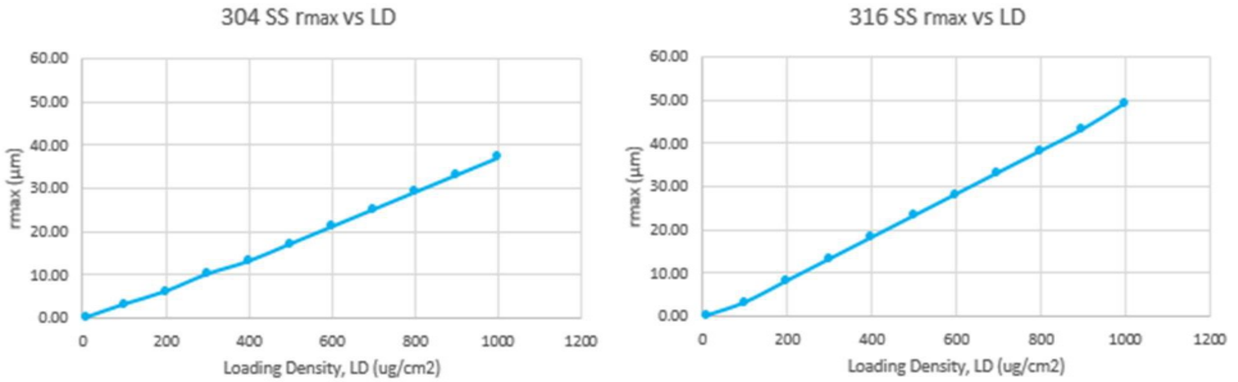

Figure 39: r_{max} vs LD for 304L (a) and 316L SS (b)

The results of r_{max} versus RH for 304L and 316L SS is shown below in Figure 40. For these results, the temperature was held constant at 25°C, Cl at 0.6 M, LD at 0.5 g/cm^2, and I/r at 0.844 A/m. These graphs show that r_{max} and RH have an exponential relationship for both 304L and 316L SS.

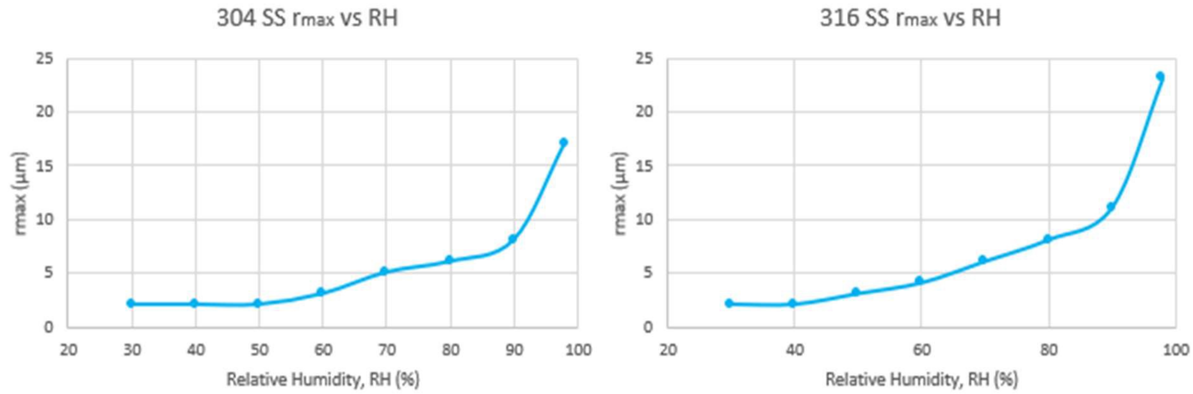

Figure 40: r_{max} vs RH for 304L (a) and 316L SS (b)

Figures 41 and 42 are temperature plots. Figure 41 shows the results of r_{max} versus LD for both alloys and Figure 42 shows the results of r_{max} vs RH for 304L and 316L SS. For Figure 41, the RH was held constant at 98%, Cl at 0.6 M, and I/r at 0.844 A/m. For Figure 42, the LD was held constant at 0.5 g/cm^2, Cl at 0.6 M, and I/r at 0.844 A/m. Figure 41 shows a direct correlation between the two whereas Figure 42 shows an exponential relationship for both materials.

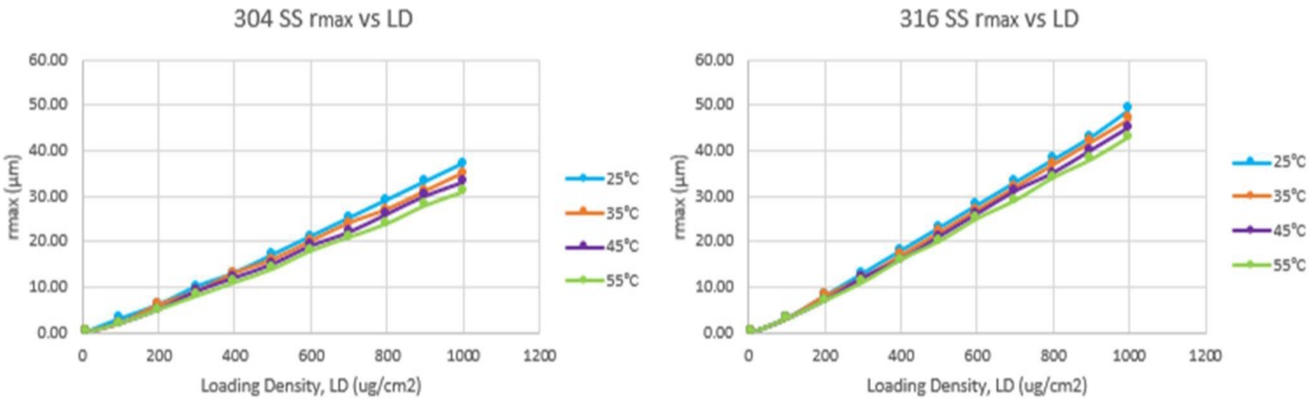

Figure 41: r_{max} vs LD for 304L (a) and 316L SS (b) at various temperatures

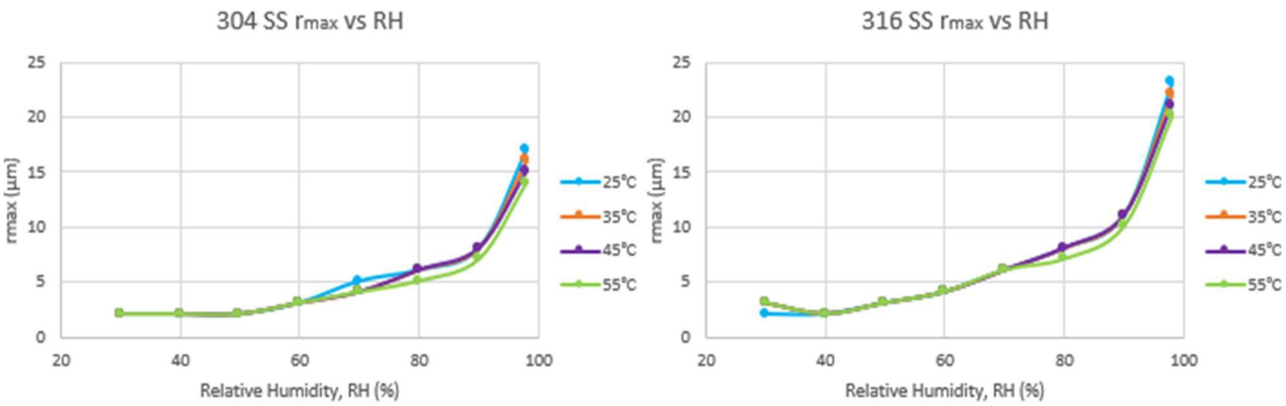

Figure 42: r_{max} vs RH for 304L (a) and 316L SS (b) at various temperatures

3.3 New Database

While writing this thesis, these calculations (shown above) were shared with OLI who discovered that the 304L SS model needed improvement and provided a new database with improved parameters. This database is not commercially available yet. Calculations for $MgCl_2$ 304L SS with the new database are shown below in Figures 43 and 44. Figure 43a shows the results of the chloride effects for $MgCl_2$ where there is a peak in the corrosion rate at ~4 M and Figure 43b shows that above a critical concentration (~4 M), the OCP falls below the E_{rp}. The results of the temperature effects on the corrosion rate, OCP, and E_{rp} can be seen below in Figure 44. These graphs show that as the temperature increases, the corrosion rate will peak around 110°C (Fig. 44a) and when the OCP falls below the E_{rp}, the critical temperature is lower for higher concentrations (Fig. 44b).

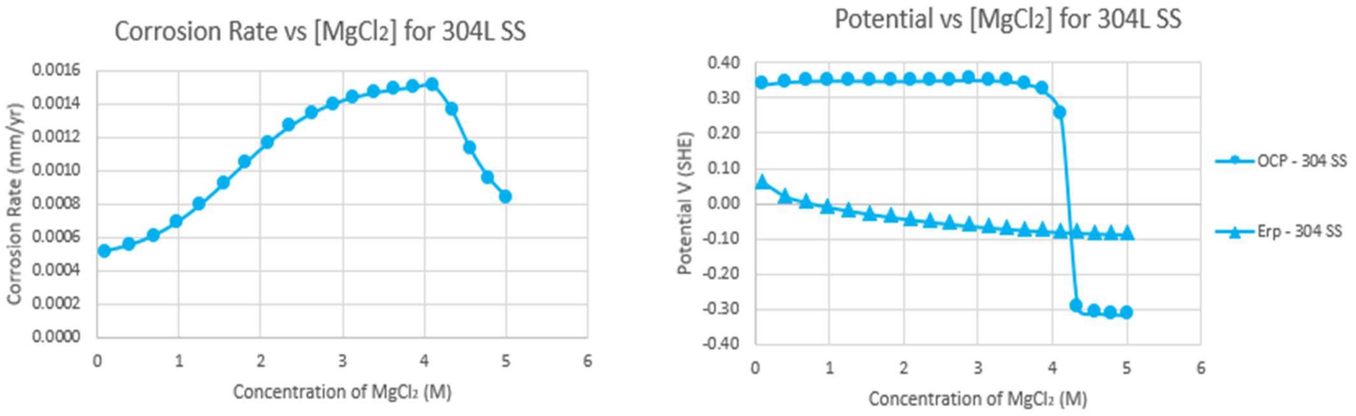

Figure 43: Corrosion rate (a) and potential (Erp and OCP) (b) vs [MgCl2] for 304L SS of the new database

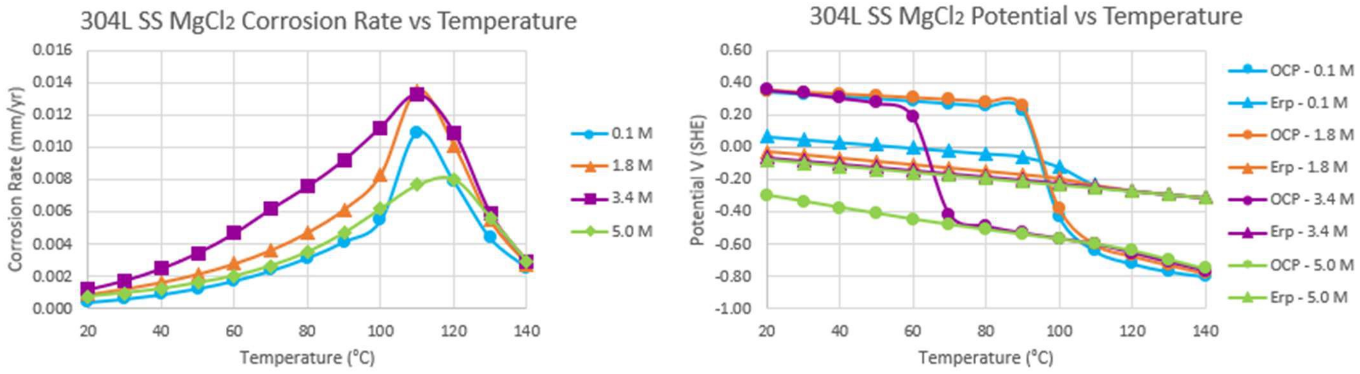

Figure 44: Corrosion rate (a) and potential (E_{rp} and OCP) (b) of $MgCl_2$ on 304L SS vs T

4. Discussion

4.1 Overview

In this section, two points will be made and discussed. The first is that only the compounds with equivalent chloride concentrations will produce the same or similar result. For example, 1.0 M $MgCl_2$ and 2.0 M NaCl both have equivalent chloride concentrations and the results are shown below in Figures 45 and 46. Figure 45 shows the OCP and E_{rp} for both concentrations for 304L and 316L SS on separate graphs. Figure 46 shows the same data but for both materials on the same graph. From these graphs, it can be seen that 1.0 M $MgCl_2$ and 2.0 M NaCl both produce almost the exact same result for both alloys, which proves that compounds with equivalent chloride concentrations will give the same or similar result.

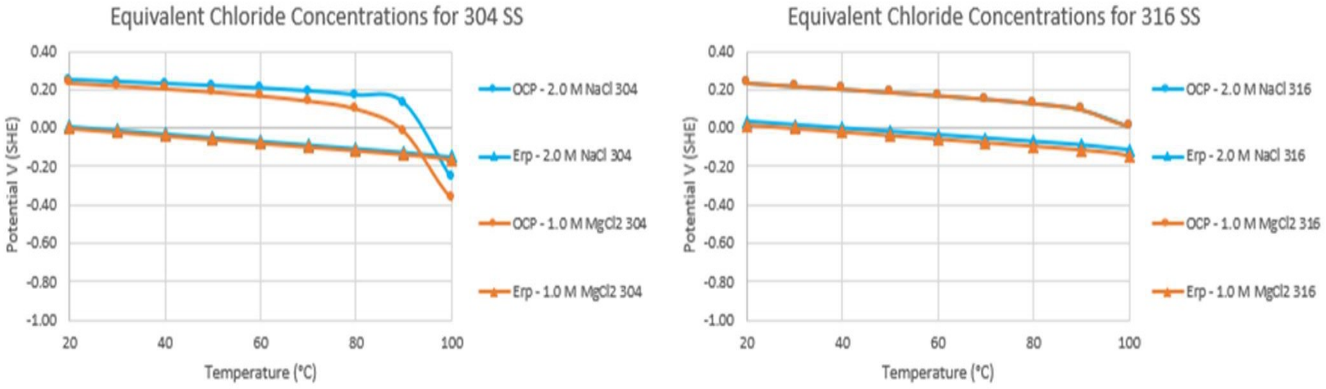

Figure 45: Potential (E_{rp} and OCP) for 1.0 M $MgCl_2$ and 2.0 M NaCl on 304L (a) and 316L SS (b) vs T

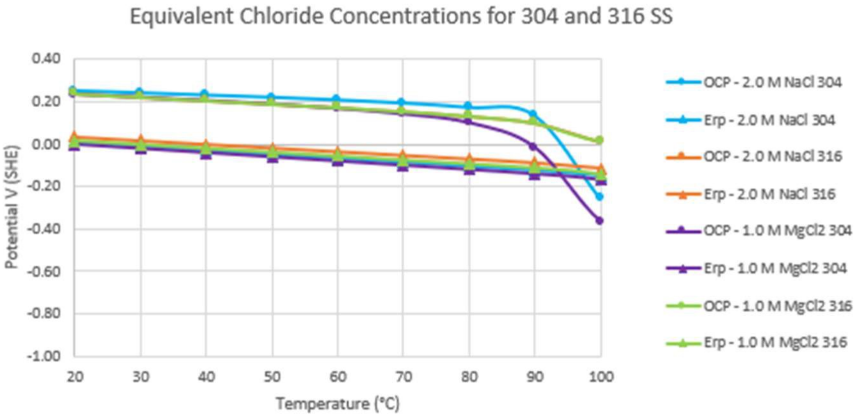

Figure 46: Potential (E_{rp} and OCP) for 1.0 M $MgCl_2$ and 2.0 NaCl on 304L and 316L SS vs T

The second important point is that the corrosion morphology is expected to change as the surface solution chemistry changes. The sharp transitions, that were seen above in the results section, in the OCP for 304L SS occur at critical, higher temperatures and will result in the OCP being lower than the Erp. Therefore, during the time the dry storage canister is at a high enough temperature (i.e., when the OCP is lower than the E_{rp}), the corrosion attack will be active, uniform corrosion, rather than pitting. This prediction is important as uniform corrosion can be managed much more easily than localized corrosion which tends to be more stochastic in location and severity.

4.2 Computational

Computations of Surface Solution Chemistry and Electrochemistry

5.4 M NaCl for 304L SS (Figures 3a,b and 4a,b) will be used as an example of the method used to interpret changes in the OCP coupled to changes in the corrosion rate and are reproduced below for convenience. Figure 3a shows the corrosion rate, and it can be seen that the corrosion rate of 304L SS in 5.4 M NaCl increased the most as the temperature increased as compared to other chloride concentrations. Figure 3b shows the OCP and Erp and the OCP for 5.4 M NaCl decreased as the temperature increased, reaching a critical temperature at which it becomes below the Erp, resulting in a sharp transition that can be seen below.

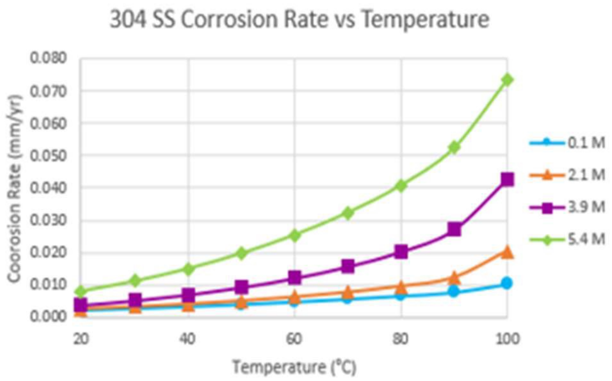

Figure 3a: Corrosion rate of NaCl on 304L SS vs T

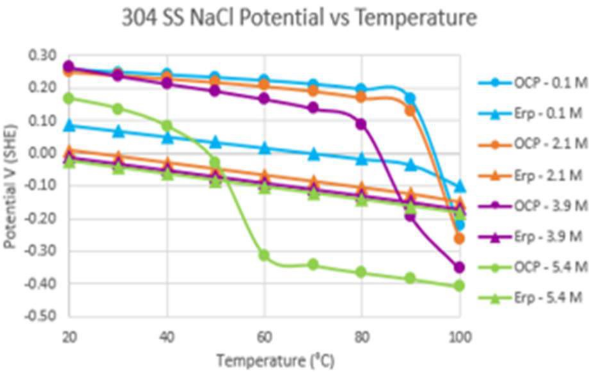

Figure 3b: Potential (E_{rp} and OCP) of NaCl on 304L SS vs T

Figure 4 shows the Evans diagrams before the sharp transition at 40°C and after the sharp transition at 80°C for 5.4 M NaCl for 304L SS that was seen in Figure 3b. When looking from Figure 4a to Figure 4b, differences in the current density and corrosion potential can be seen. When there is an increase in passive current density where it exceeds the diffusion-limited oxygen reduction reaction for 5.4 M NaCl on 304L SS, the corrosion potential drops, as per the Mixed Potential Theory. When the corrosion rate increases and the OCP becomes more negative, as can be seen in 5.4 M NaCl for 304L SS, it can be concluded that changes in the anodic reaction kinetics are the dominant cause. What this means is that the change that controls the corrosion rate and OCP are driven by changes in one of the reactions relative to the others, but it does not preclude the other reactions from changing at all.

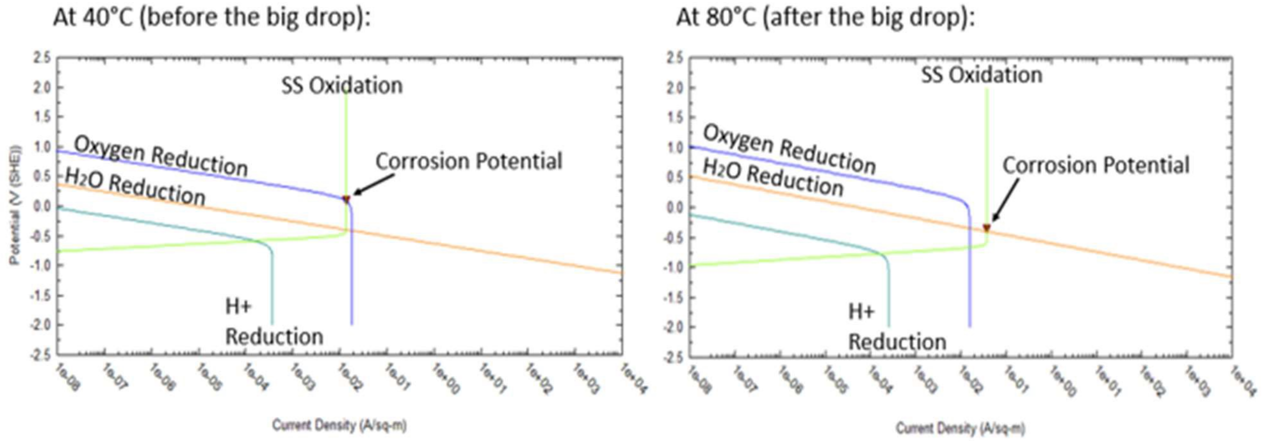

Figure 4: Evans diagrams of 5.4 M NaCl on 304L SS at 40°C before (a) and 80°C after (b) sharp transition

For the results of the chloride solutions, sharp transitions occurred in the OCP for 304L SS over a narrow temperature range for each species. In the case of NaCl, when there is an increase in passive current density to the point that it exceeds the oxygen reduction reaction, the corrosion potential drops into active dissolution region (Fig. 4). This drop in corrosion potential means that activation of 304L SS for NaCl by higher temperature changes the attack from pitting to active, uniform corrosion. $MgCl_2$ (Fig. 8) and $CaCl_2$ (Fig. 12) showed that when there is an increase in passive current density by greater than 10x and a decrease in the oxygen reduction reaction, it will cause the corrosion potential to drop and the corrosion rate to increase. KCl (Fig. 16) and NH_4Cl (Fig. 20) showed that the corrosion potential drops and the anodic current potential increases. This was the same for $MgCl_2$ (Fig. 6) and $CaCl_2$ (Fig. 10) when both showed a peak in the corrosion rate over a concentration range and it was also the same for KCl (Fig. 15) and NH_4Cl (Fig. 19) when both showed a peak in the corrosion rate for over a temperature range. For all the chloride solutions, the OCP will always be lower than the E_{rp} when the compound is 100% saturated because there will be no passivity so there cannot be any localized corrosion.

For the results of the nitrate and sulfate solutions, sharp transitions occurred in the corrosion potential over a temperature range for KNO_3 (Fig. 24), $NaNO_3$ (Fig. 28), and Na_2SO_4 (Fig. 35) where the corrosion potential drops and the anodic current density increases. For KNO_3, $NaNO_3$, Na_2SO_4, and $CaSO_4$, there was no repassivation potential calculated. The results of the stoichiometric solutions showed that the corrosion potential of 304L SS is lower than that of 316L SS because stoichiometric solutions of 316L SS have a lower pH and cause the 316L SS to corrode faster than the 304L SS in its stoichiometric solution.

Computations of Maximum Pit Sizes

For the results of the maximum pit sizes, it can be seen that r_{max} has a positive direct relationship with LD, a positive exponential relationship with RH, and a negative exponential relationship with I/r, including at increasing temperatures for LD and RH.

Ramifications for Dry Storage Canisters

Figures 47a and 47b, from C.R. Bryan et al., are shown below. Figure 47a shows the modeled canister surface temperature at different initial heat loads and Figure 47b shows the relative humidity as a function of time. As seen with the results of the maximum pit size calculations (shown in Figures 38 – 42), it can be determined that the maximum pit size will increase as the temperature and RH decreases over time. Corrosion can start when the deliquescent RH for seawater is reached, which is about 35%. When looking at Figure 47b, it can be seen that corrosion will occur around 100 years. Based on this graph, the maximum pit size will increase over time, but it will not hit the maximum pit size because it does not reach ~75% RH during this time period.

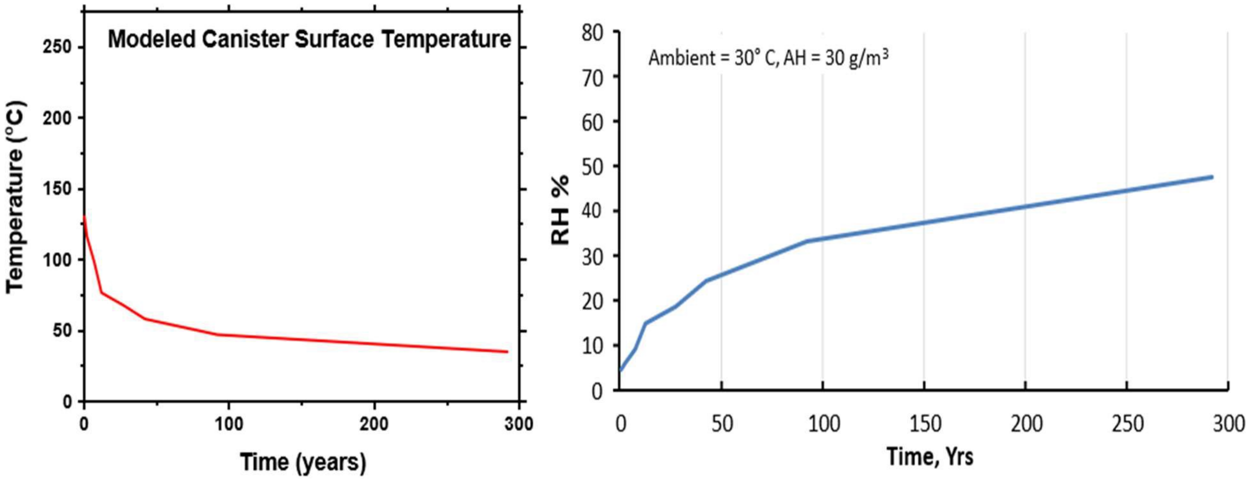

Figure 47: T (a) and RH (b) vs t[22]

4.3 Sensitivity of Results to Parameterization

The two databases (denoted as "DB" in the graphs) will be compared using the results of $MgCl_2$ for 304L SS shown below in Figures 48 – 51. Figure 48 compares the corrosion rate, OCP, and E_{rp} for both databases. It can be seen in Figure 48a that the corrosion rates with the new database are lower in comparison to the old database and that with the new database, the corrosion rate will increase initially and then decrease at higher $MgCl_2$ concentrations. Figure 48b shows that the OCP for the new database is larger than it is for the old database and that the E_{rp} stayed the same for both databases. Figure 48 can be understood by looking at the polarization curves of before and after the peak for the new database, shown below in Figure 49, because the main cathodic reaction is the oxygen reduction so as the concentration of $MgCl_2$ increases, the limiting current density decreases. Figure 50 displays the corrosion rate with temperature for both databases and while the old database indicates that there is a switching of the corrosion rate order as the temperature increases, this is not the case with the new database because the limiting current density increases with concentration. Figure 51 shows the OCP and E_{rp} for both databases and although there is some variation, it can be seen that the same trend is followed. Therefore, it can be determined that the 304L SS model, and subsequent maximum pit size predictions, are sensitive to the parameters used. The details of the parameters for the new database are not known as that is proprietary information and the database for 316L SS needs revision and is currently underway.

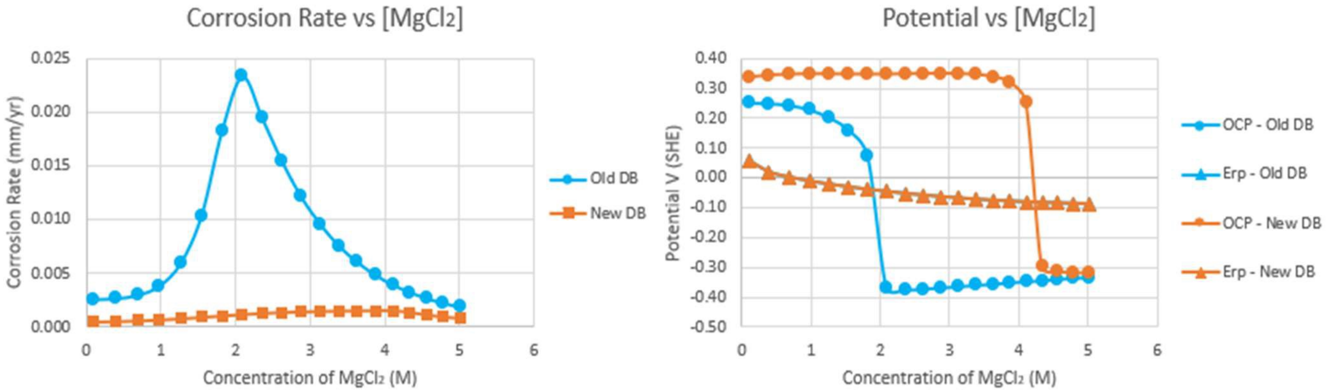

Figure 48: Corrosion rate (a) and potential (E_{rp} and OCP) (b) vs [$MgCl_2$] on 304L SS for both databases

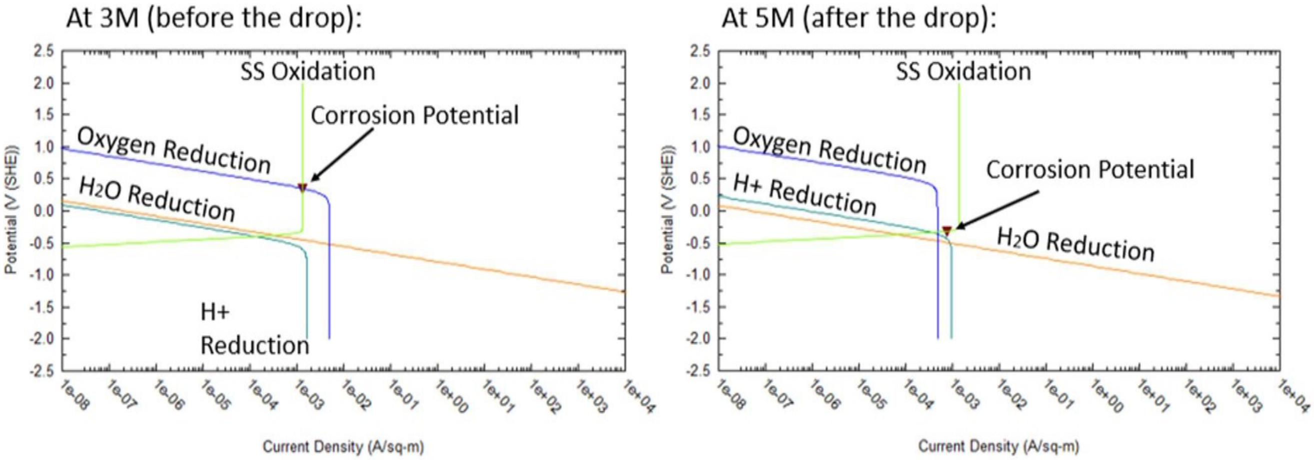

Figure 49: Evans diagrams of 3 M (a) and 5 M (b) $MgCl_2$ on 304L SS for new database

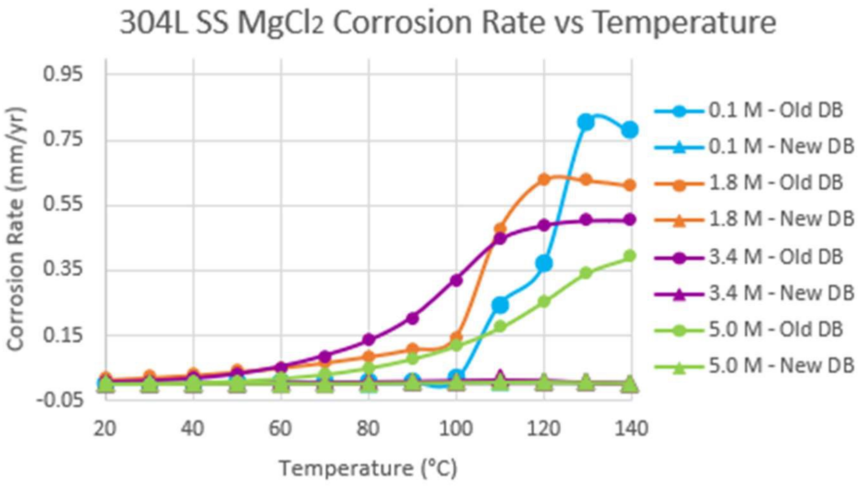

Figure 50: Corrosion rate of $MgCl_2$ on 304L SS vs T for both databases

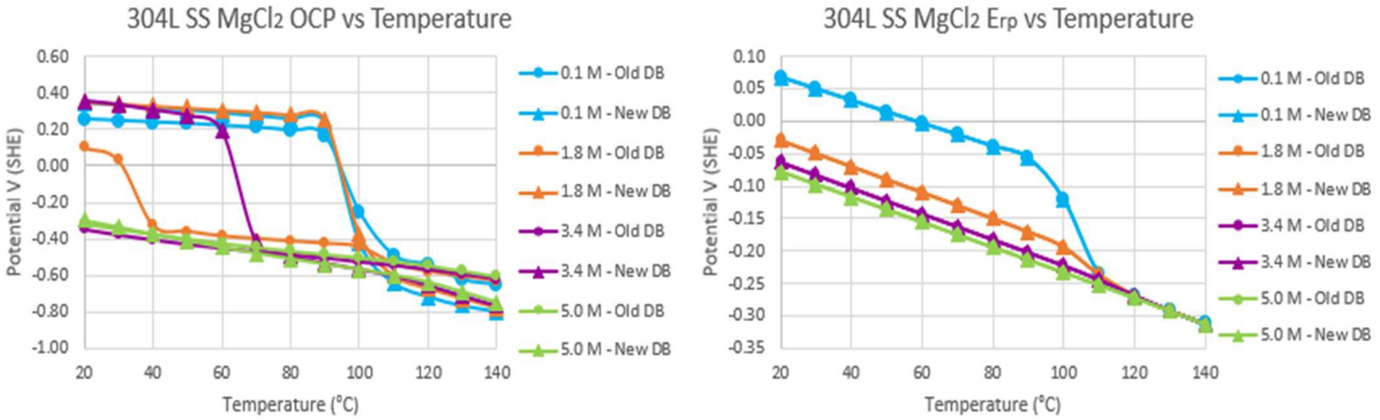

Figure 51: OCP (a) and E_{rp} (b) of $MgCl_2$ on 304L SS vs T for both databases

4.4 Limitations

While using OLI Studio: Corrosion Analyzer^{TM}, several limitations were discovered. The database used, which is currently the most comprehensive, is only limited to 6,000 species and may not have the data for certain compounds of interest. OLI was also limited at higher temperatures as it was unable to determine the values for the corrosion rate, OCP, and E_{rp} for most compounds during a temperature study in this work.

5. Conclusions

The OLI computational results show that compounds that have equivalent chloride concentrations will produce the same or similar result, such as 1 M $MgCl_2$ and 2 M NaCl. As the surface solution chemistry changes, so does the corrosion morphology. At a high enough temperature, sharp transitions in the OCP for 304L SS will occur and will result in the OCP being lower than the E_{rp}. As previously stated, conditions under which the OCP is lower than the E_{rp}, localized corrosion would not be expected to occur because when the canister reaches a high enough temperature, it will change the corrosion attack from pitting to active, uniform corrosion. These data are required as input for the maximum pit calculations for the dry storage canisters. Additionally, in simple salt solutions, 316L SS is more resistant to increased chlorides at increased temperatures than 304L SS, as expected. 316L SS corrodes faster in its stoichiometric solutions because the pH is lower than that of 304L SS. Lastly, by comparing the old and new database, it shows that the model used for 304L SS and the inputs for the maximum pit size predictions are sensitive to the parameters used.

6. Future Work

Once the new database is commercially available for both 304L and 316L SS, concentration and temperature studies need to be calculated for NaCl and $MgCl_2$ for both alloys. Additionally, experimental validation is needed for future work. A set of cases that can be done experimentally to show the range of behavior observed are: (1) corrosion rate versus the concentration of NaCl (0.1 – 5.4 M) at 25°C for both alloys, (2) corrosion rate versus temperature (20 – 100°C) for 0.1 M, 2.1 M, 3.9 M, and 5.4 M NaCl for both alloys, (3) OCP and E_{rp} versus NaCl concentration (0.1 – 5.4 M) for both alloys at 25°C, (4) OCP and E_{rp} versus temperature (20 – 100°C) for 0.1 M, 2.1 M, 3.9 M, and 5.4 M NaCl for both alloys, (5) corrosion rate versus the concentration of $MgCl_2$ (0.1 – 5.0 M) for both alloys at 25°C, (6) corrosion rate versus temperature (20 – 140°C) for 0.1 M, 1.8 M, 3.4 M, and 5.0 M $MgCl_2$ for both alloys, (7) OCP and E_{rp} versus $MgCl_2$ concentration (0.1 – 5.0 M) at 25°C for both alloys, and (8) OCP and E_{rp} versus temperature (20 – 140°C) for 0.1 M, 1.8 M, 3.4 M, and 5.0 M $MgCl_2$ for both alloys. By conducting this set experimentally, it can be used to validate the computational results and/or provide more data to improve the parameters for the new OLI database.

7. Appendix

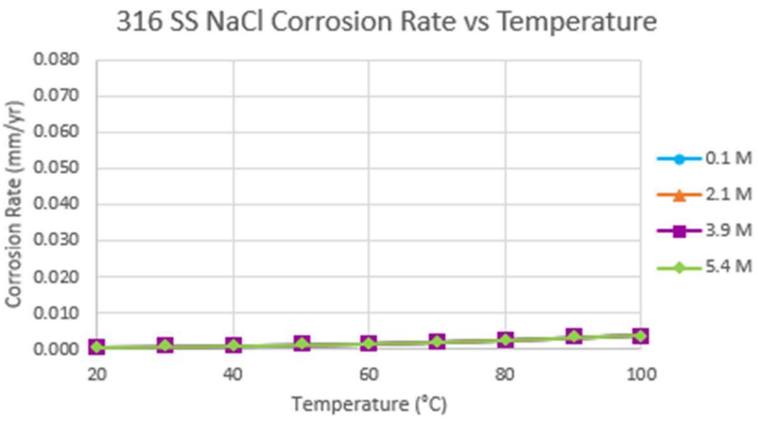

Figure A: Corrosion rate of NaCl on 316L SS vs T

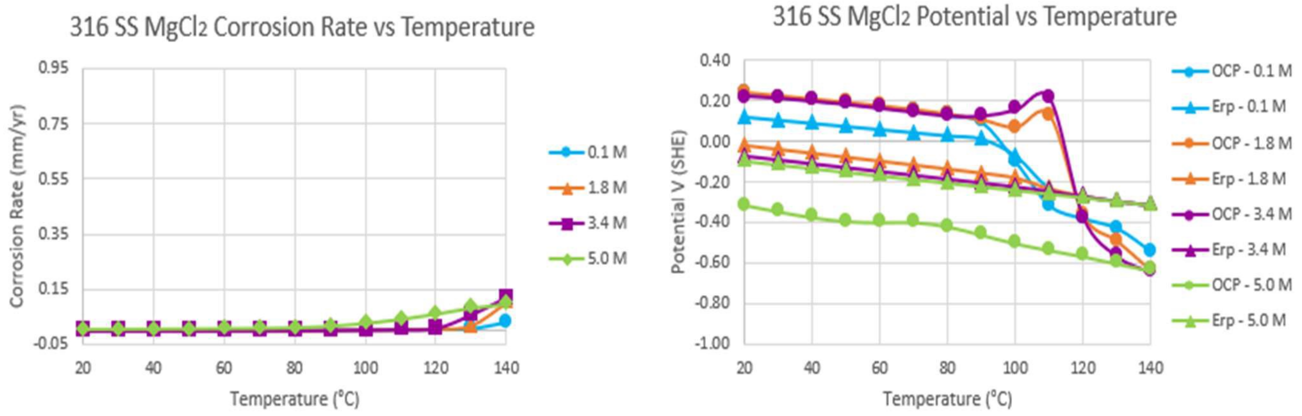

Figure B: Corrosion rate (a) and potential (E_{rp} and OCP) (b) of $MgCl_2$ on 316L SS vs T

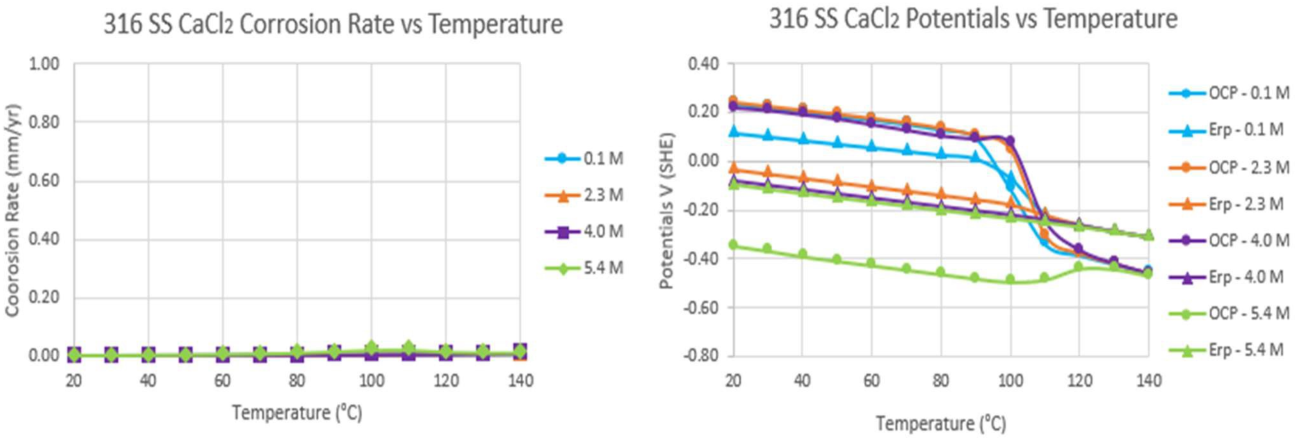

Figure C: Corrosion rate (a) and potential (E_{rp} and OCP) (b) of $CaCl_2$ on 316L SS vs T

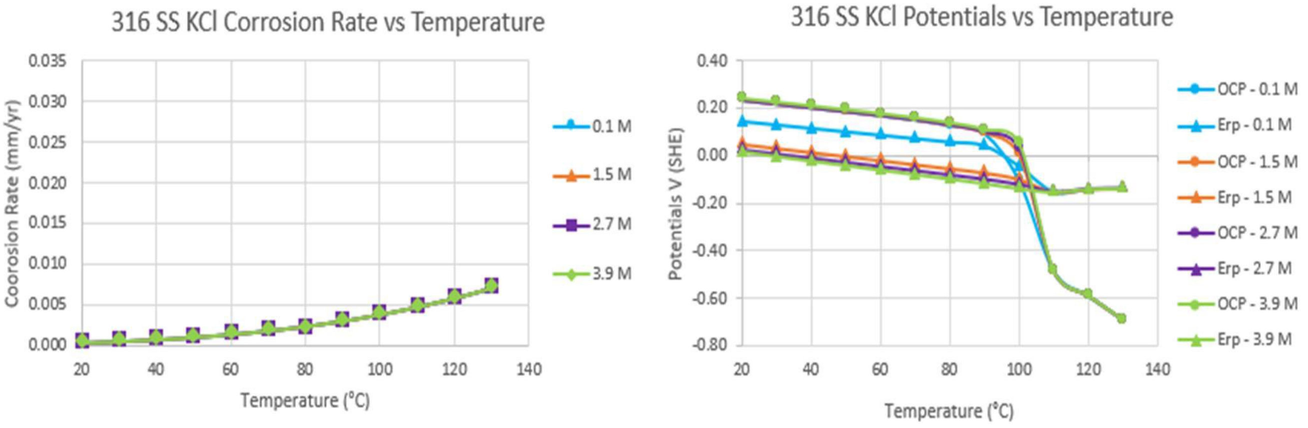

Figure D: Corrosion rate (a) and potential (E_{rp} and OCP) (b) of KCl on 316L SS vs T

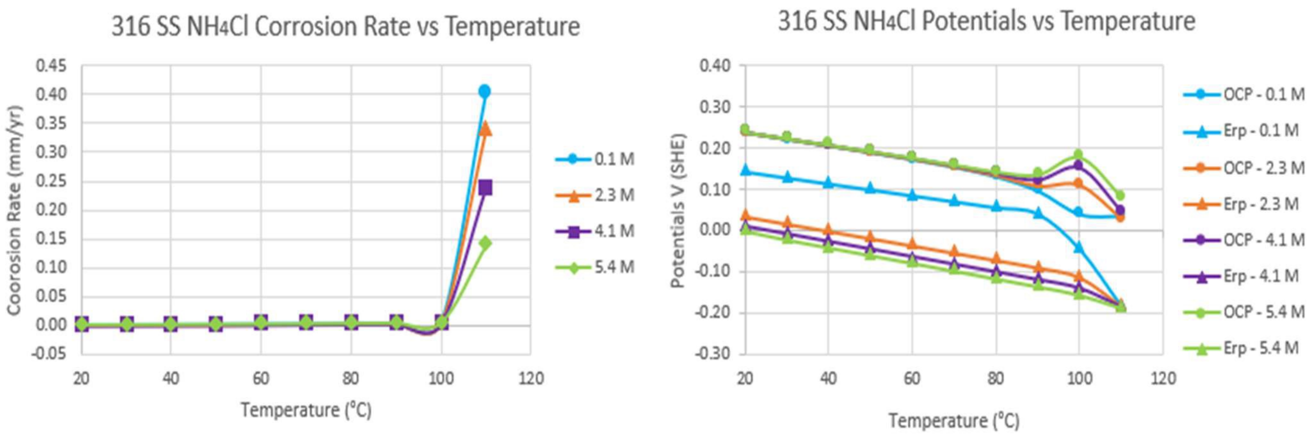

Figure E: Corrosion rate (a) and potential (E_{rp} and OCP) (b) of NH_4Cl on 316L SS vs T

8. References

1. *Less Electricity Was Generated by Coal Than Nuclear in the United States in 2020*. U.S. Energy Information Administration. (n.d.). https://www.eia.gov/todayinenergy/detail.php?id=47196
2. *What Is Spent Nuclear Fuel?* United States Nuclear Regulatory Commission. (n.d.). www.nrc.gov/reading-rm/basic-ref/students/science-101/what-is-an-spent-fuel.html.
3. Mintz, T. S., Miller, L., Pan, Y.-M., Oberson, G., He, X., Pabalan, R., Caseres, L., & Dunn, D. (2018). Coastal Salt Effects on the Stress Corrosion Cracking of Type 304 Stainless Steel. *Sereal Untuk*, *51*(1), 51.
4. Frankel, G. S. (1998). Pitting Corrosion of Metals: A Review of the Critical Factors. *Journal of The Electrochemical Society*, *145*(6), 2186–2198. https://doi.org/10.1149/1.1838615
5. Vehovar, L., & Tandler, M. (2001). Stainless steel containers for the storage of low and medium level radioactive waste. *Nuclear Engineering and Design*, *206*(1), 21–33. https://doi.org/10.1016/S0029-5493(00)00443-X
6. Zhang, Y., Cook, A. J. M. C., Padovani, C., Zhou, S., & Turnbull, A. (2020). Atmospheric stress corrosion crack growth rates of 316 L stainless steel for nuclear waste containment. *Corrosion Science*, *177*, 109008. https://doi.org/10.1016/j.corsci.2020.109008
7. Ahmad, Z. (2006). *Principles of Corrosion Engineering and Corrosion Control*. 57–119. https://www.sciencedirect.com/science/article/pii/B9780750659246500040
8. *Cathode and Anode*. BYJU'S. (n.d.). https://byjus.com/chemistry/cathode-and-anode/.
9. *Mixed Potential Theory*. (n.d.) https://www.uobabylon.edu.iq/eprints/publication_12_18241_228.pdf
10. Chen, Z. Y., & Kelly, R. G. (2010). Computational Modeling of Bounding Conditions for Pit Size on Stainless Steel in Atmospheric Environments. *Journal of The Electrochemical Society*, *157*(2), C69. https://doi.org/10.1149/1.3261803
11. *General Corrosion*. Corrosionpedia. (n.d.). https://www.corrosionpedia.com/definition/589/general-corrosion

12. *Uniform Corrosion*. AMPP. (n.d.). https://www.ampp.org/resources/impact/corrosion-basics/group-1/uniform-corrosion
13. Frankel, G. S., & Sridhar, N. (2008). Understanding localized corrosion. *Materials Today*, *11*(10), 38–44. https://doi.org/10.1016/S1369-7021(08)70206-2
14. Woldemedhin, M. T., Srinivasan, J., & Kelly, R. G. (2015). Effects of environmental factors on key kinetic parameters relevant to pitting corrosion. *Journal of Solid State Electrochemistry*, *19*(12), 3449–3461. https://doi.org/10.1007/s10008-015-2816-9
15. Katona, R. M., Carpenter, J., Schindelholz, E. J., & Kelly, R. G. (2019). Prediction of Maximum Pit Sizes in Elevated Chloride Concentrations and Temperatures. *Journal of The Electrochemical Society*, *166*(11), C3364–C3375. https://doi.org/10.1149/2.0451911jes
16. *Galvanic Couple*. Corrosionpedia. (n.d.). https://www.corrosionpedia.com/definition/569/galvanic-couple
17. Woldemedhin, M. T., Shedd, M. E., & Kelly, R. G. (2014). Evaluation of the Maximum Pit Size Model on Stainless Steels under Thin Film Electrolyte Conditions. *Journal of The Electrochemical Society*. https://doi.org/10.1149/2.023408jes
18. Anderko, A., & Young, R.D. (2000). Model for Corrosion of Carbon Steel in Lithium Bromide Absorption Refrigeration Systems. *CORROSION*, *56*(5), 543-555. https://doi.org/10.5006/1.3280559
19. Anderko, A., McKenzie, P., & Young, R.D. (2001). Computation of Rates of General Corrosion Using Electrochemical and Thermodynamic Models. *CORROSION*, *57*(3), 202-213. https://doi.org/10.5006/1.3290345
20. *OLI Studio: Corrosion Analyzer*. OLI Systems. (n.d.). https://www.olisystems.com/products-corrosion-analyzer.
21. *OLI Technology.* OLI Systems. (n.d.). https://www.olisystems.com/technology.
22. C.R. Bryan, A.W. Knight, R.M. Katona, et al., Physical and chemical properties of sea salt deliquescent brines as a function of temperature and relative humidity, *Science of the Total Environment* (2021).
23. Chen, Z.Y., Cui, F., & Kelly, R.G. (2008). Calculations of the Cathodic Current Delivery Capacity and Stability of Crevice Corrosion under Atmospheric Environments. *Journal of The Electrochemical Society*, *155*(7), C360-C368.